nature communications

Article

https://doi.org/10.1038/s41467-025-67119-3

Targeting chaperone-mediated autophagy inhibits properties of glioblastoma stem cells and restores anti-tumor immunity

Received: 22 January 2025

Accepted: 20 November 2025

Yonghua Li[1,6], Min Sheng[1,6], Weijie Li[1,6], Simin Liu[2,6], Botao Wang[1], Bing Liu[1], Mei Luo[1], Xiao Zhou[1], Qiaoxi Xia[1], Shihong Hong[1], Ziyuan Zheng[1], Shi-Yuan Cheng[3], Xiaobing Jiang[2] ✉, Junjun Li[2] ✉ & Tianzhi Huang[1,4,5] ✉

Chaperone-mediated autophagy (CMA) is a selective autophagic process essential for maintaining cellular quality and responding to stress. Dysregulation of the CMA pathway is increasingly recognized in various cancers, yet the mechanisms behind CMA hyperactivation in cancer cells remain unclear. Here, we show that CMA is upregulated in patient-derived glioblastoma stem cells (GSCs), indicated by a significant increase in the lysosomal abundance of the CMA receptor, lysosome-associated membrane protein 2 A (LAMP2A). This increase results from MST4-mediated phosphorylation of LAMP2A, enhancing its stability and promoting homotrimer formation while inhibiting degradation by Cathepsin A. CMA supports GSC proliferation and self-renewal by activating mTORC1 through the selective degradation of its negative regulators, TSC1 and TSC2. Additionally, CMA is involved in epigenetic silencing of the cGAS-STING pathway, promoting tumor immune escape via lysosomal degradation of the DNA demethylase TET3. Inhibition of CMA synergizes with immune checkpoint therapy in glioblastoma models, highlighting a potential therapeutic target.

Glioblastoma (GBM) represents the most prevalent and aggressive primary malignancy of the central nervous system in adults, classified among the most lethal cancers[1]. Current therapeutic approaches for GBM encompass surgical excision, radiotherapy, and the use of temozolomide (TMZ) as an adjunctive chemotherapy agent. Nonetheless, the prognosis for GBM patients remains dismal, with a median survival duration of roughly 14 months and a mere 5% survival rate at five years[2]. Furthermore, immune checkpoint inhibitor (ICI) therapies have failed to improve the overall survival in GBM patients[3]. A prior study has identified glioblastoma stem cells (GSCs) within GBM tumors, noted for their robust self-renewal and differentiation capabilities, which lead to the generation of a diverse array of cancer cell types[4]. Additionally, GSCs exhibit resistance to both radiotherapy and chemotherapy while also contributing to immune evasion, which are critical factors underlying treatment failure and GBM recurrence[5–7]. Therefore, the advancement of targeted therapies aimed at GSCs is essential for the efficacious management of GBM.

Autophagy plays a crucial role in the proteostasis network, ensuring cellular homeostasis. Various autophagic pathways are present in most mammalian cells, differing primarily in their mechanisms

---

[1]State Key Laboratory of Cellular Stress Biology, School of Life Sciences, Women and Children's Hospital, Faculty of Medicine and Life Sciences, Xiamen University, Xiamen, Fujian, China. [2]Department of Neurosurgery, Union Hospital, Tongji Medical College, Huazhong University of Science and Technology, Wuhan, Hubei, China. [3]The Ken and Ruth Devee Department of Neurology, Lou and Jean Malnati Brain Tumor Institute Northwestern Medicine, The Robert H. Lurie Comprehensive Cancer Center, Simpson Querrey Institute for Epigenetics, Northwestern University Feinberg School of Medicine, Chicago, IL, USA. [4]Shenzhen Research Institute of Xiamen University, Shenzhen, Guangdong, China. [5]State Key Laboratory of Vaccines for Infectious Diseases, Xiang An Biomedicine Laboratory, Xiamen University, Xiamen, Fujian, China. [6]These authors contributed equally: Yonghua Li, Min Sheng, Weijie Li, Simin Liu. ✉e-mail: 2004xh0835@hust.edu.cn; ljj19891105@126.com; huangtianzhi@xmu.edu.cn

for transporting substrates to the lysosomal compartment[8]. In contrast to macroautophagy, which facilitates the bulk translocation of proteins and organelles to lysosomes for degradation[9], chaperone-mediated autophagy (CMA) selectively targets a specific subset of cytosolic proteins characterized by KFERQ-like motifs[10,11]. Upon recognition of these motifs by heat shock cognate 71 kDa protein (HSC70), the substrate is translocated to the lysosomal membrane's surface[12], where it interacts with lysosome-associated membrane protein type 2 A (LAMP2A), which has been identified as a limiting factor for CMA efficacy[13]. The binding of the substrate to the cytosolic tail of LAMP2A induces LAMP2A oligomerization, forming a translocation complex that facilitates the internalization of substrates into lysosomes for subsequent degradation[14,15]. CMA is implicated in the degradation of both defective proteins for quality control and intact proteins to modulate their functions, thereby coordinating various intracellular processes, including aging, lipid and glucose metabolism, cell signalling, cell cycle, stem cell functionality and immune responses[10,16–20]. Despite its established role, the regulatory networks governing CMA activity remain incompletely characterized[10,21]. Notably, while macroautophagy contributes to cancer stem cell malignancy[22,23], CMA-specific receptor LAMP2A demonstrates elevated expression in patient-derived GSCs[17], suggesting potential differential roles in specialized cell populations that require further elucidation.

MST4 (also known as STK26), a constituent of the Mammalian Sterile 20-Like Kinase (MST) family[24], is integral to numerous cellular physiological processes via substrate phosphorylation[25]. It has been implicated in the pathogenesis of colorectal cancer by phosphorylating β-catenin, which results in its accumulation and full activation[26]. Additionally, MST4 is recognized for phosphorylating ATG4B, thereby initiating macroautophagy, which enhances cell survival and tumorigenic potential of GSCs[27]. Nonetheless, the involvement of MST4 in tumor-associated CMA remains to be elucidated.

The cyclic GMP-AMP synthase (cGAS)-stimulator of interferon genes (STING) signaling pathway is a crucial component of the innate immune response, significantly contributing to anti-tumor immunotherapy[28]. Cytoplasmic DNA acts as a danger signal, which is recognized by cGAS, leading to the synthesis of the second messenger cGAMP[29,30]. This process initiates the activation of the STING-TBK1-IRF3-type I interferon (IFN) signaling cascade[31,32]. The stimulation of the cGAS-STING pathway through various modalities, including radiotherapy and chemotherapy, is regarded as a promising combinatorial approach with ICIs and other immuno-oncological therapeutics[33,34]. However, in numerous tumors, the promoters of cGAS and STING are frequently hypermethylated, leading to the silencing of this pathway[35,36]. The epigenetic regulatory mechanisms governing the expression of cGAS and STING genes remain inadequately understood.

In this work, we elucidate the critical role of the MST4-LAMP2A signaling axis in regulating CMA activity, self-renewal capacity, and tumorigenic potential of GSCs, alongside its ramifications for anti-tumor immunity. Mechanistically, phosphorylation of LAMP2A at residues T40, S97, and T136 by MST4 is demonstrated to reinforce LAMP2A stability, and thereby elevating CMA activity. This enhancement subsequently promotes the proliferation and malignancy of GSCs. Furthermore, we identify a function of CMA as an intrinsic regulator of anti-tumor immune responses, suggesting a promising therapeutic avenue focused on targeting CMA for GBM treatment.

Results

Elevated level of CMA in GSCs is associated with increased LAMP2A abundance in lysosomes

We employed a photoactivatable CMA reporter (PA-mCherry-KFERQ) to visualize and quantify CMA activity by counting the fluorescent puncta per cell. This occurs when the fluorescent CMA substrate protein, fused with a KFERQ-like motif, is delivered to CMA-active lysosomes by HSC70, resulting in a transition from a diffuse to a punctate distribution. In contrast, bulk lysosomal degradation pathways, such as macroautophagy, target substrates lacking the KFERQ motif and do not produce fluorescent puncta under this assay condition[37]. We found that patient-derived GSCs exhibited significantly higher baseline CMA activity than conventional GBM cell lines (Fig. 1a). Lysosomes purified from GSCs demonstrated a significant enhancement in both the binding affinity for and uptake of the model CMA substrate, glyceraldehyde-3-phosphate dehydrogenase (GAPDH)[38], in comparison to those derived from conventional GBM cell lines (Fig. 1b). In agreement with increased CMA activity in the lysosomes from GSCs, the levels of known CMA substrates, including MEF2D and GAPDH[38,39], were markedly elevated in GSCs following the inhibition of lysosomal proteolysis through treatment with lysosomal protease inhibitors (leupeptin and ammonium chloride (NH_4Cl), LN). In contrast, such an increase was not detected in conventional GBM cells. Additionally, inhibition of macroautophagy via 3-methyladenine (3-MA) or proteasomal inhibition with MG132 did not alter the expression of MEF2D and GAPDH (Fig. 1c). To examine whether CMA activity is required for stemness maintenance of GSCs, we cultured GSCs in medium containing serum to induce differentiation. As expected, differentiated-GSCs (DGCs) exhibited a decrease in CMA flux (Fig. 1d), alongside diminished expression of pluripotency markers such as CD44 and ALDH1A3 and upregulation of the differentiation marker Tuj1 (Supplementary Fig. 1a). Collectively, these results indicated that CMA is upregulated in GSCs.

Subsequently, we aimed to elucidate the mechanisms underlying the upregulation of CMA in GSCs. We performed isolation of lysosomal fractions from both GSCs and their corresponding DGCs, revealing that lysosomes from GSCs exhibited a higher abundance of the CMA receptor, LAMP2A, compared to those from DGCs. In contrast, the levels of other established CMA components, such as a subset of chaperones (HSC70) and co-chaperones (HSP40 and HSP90), as well as lysosome-associated membrane protein 1 (LAMP1), remained constant throughout differentiation (Fig. 1e). GSC cell lines exhibited elevated levels of LAMP2A in both total cell lysate and lysosomal fractions when compared to conventional non-GSC cell lines and DGCs, even though the mRNA expression levels of *LAMP2A* were similar across these cellular types (Supplementary Fig. 1b-d). Collectively, these findings indicated that the elevated CMA activity in GSCs correlates with an increased abundance of LAMP2A in the lysosome.

To examine the biological implications of CMA in GSCs, we employed two distinct short hairpin RNAs (shRNAs) to downregulate endogenous LAMP2A in M83 and 456 cell lines. The knockdown (KD) of LAMP2A resulted in a pronounced upregulation of MEF2D (Supplementary Fig. 1e), and led to a reduction in GSC proliferation and sphere-forming capacity in vitro (Supplementary Fig. 1f, g), while significantly inhibiting intracranial tumor growth in athymic nude mice, thereby improving the overall survival (Supplementary Fig. 1h, i). Subsequently, we introduced an shRNA-resistant LAMP2A-WT (wild-type) and a functional mutant LAMP2A (LAMP2A-4A) that was deficient for substrate binding[40], into GSC M83 and 456 cells where endogenous LAMP2A was depleted. Our findings demonstrated that the reintroduction of exogenous LAMP2A-WT, but not the LAMP2A-4A mutant, effectively reversed the effects of LAMP2A KD on CMA activity (Supplementary Fig. 1j), GSC proliferation, and sphere formation ability in vitro (Fig. 1f and Supplementary Fig. 1k), as well as tumorigenicity in the brains of athymic nude mice (Fig. 1g, h), thus shortening the survival of mice (Fig. 1i). Taken together, these results indicated that CMA is required for GSC stemness and tumorigenicity.

MST4-mediated LAMP2A phosphorylation increased the stability of LAMP2A at the lysosomal membrane

Subsequently, we examined the underlying mechanisms contributing to the increased level of LAMP2A detected in GSCs. The

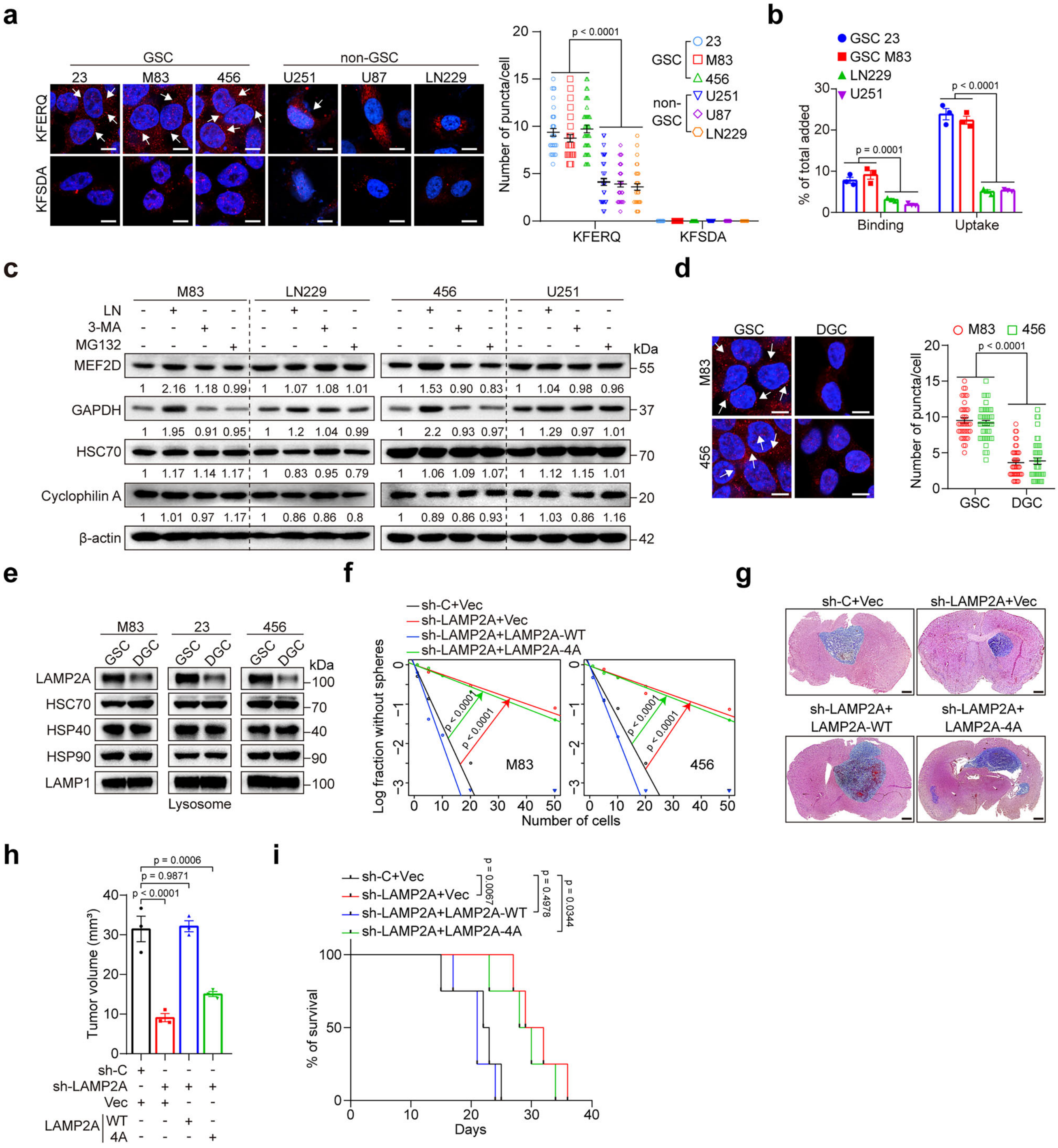

Fig. 1 | The elevated CMA activity in GSCs correlates with lysosomal LAMP2A abundance. **a** Representative images (left) and quantitative analysis (right) of CMA flux, indicated by the number of KFERQ puncta, in GSC and non-GSC cells stably expressing PAmCherry-KFERQ or PAmCherry-KFSDA (a mutant KFERQ sequence that cannot be recognized by HSC70). *n* = 40 randomly selected cells. Scale bar, 10 μm. **b** In vitro binding and uptake assay of GAPDH by the lysosome in GSC and non-GSC cells. *n* = 3 independent experiments. **c** Immunoblotting (IB) analyses for indicated proteins after treating with 10 μM MG132, 5 mM 3-MA, or LN (10 μM leupeptin and 20 mM NH_4Cl) in GSC cells (M83 and 23) and non-GSC cells (LN229 and U251), respectively. Band intensities of indicated proteins were quantified using Image J, normalized to β-actin. *n* = 3 independent experiments. **d** Representative images (left) and quantification (right) of CMA activity detection by KFERQ puncta numbers in GSCs (M83 and 456) and their corresponding DGCs. *n* = 40 randomly selected cells. Scale bar, 10 μm. **e** IB analyses for LAMP2A and CMA-associated chaperone proteins (HSC70, HSP40 and HSP90) in lysosomes isolated from the indicated GSCs and DGCs, with LAMP1 serving as a lysosomal marker. **f** Sphere-forming frequency of GSC M83 and 456 cells with indicated modifications. sh-C, control for knock down. Vec, a control vector. WT, wide-type. Representative H&E images of mouse brain sections (**g**) and quantitative analysis of tumor volume (**h**) from athymic (BALB/c Nude) mice intracranially implanted with the GSC M83 cells with indicated modifications. *n* = 3 mice per group. Scale bar, 1.0 mm. **i** Kaplan-Meier survival curves of athymic (BALB/c Nude) mice intracranially transplanted with GSC M83 cells with indicated modifications. *n* = 4 mice per group. Data are presented as the means ± S.E.M. All the experiments showed consistent results in three independent biological replicates. Statistical significance was assessed using one-way ANOVA with Tukey's multiple comparisons test (**a, b, d**), two-sided likelihood ratio test (**f**), one-way ANOVA with Dunnett's multiple comparisons test (**h**) or log-rank test (**i**). ns, not significant. Source data are provided as a Source Data file.

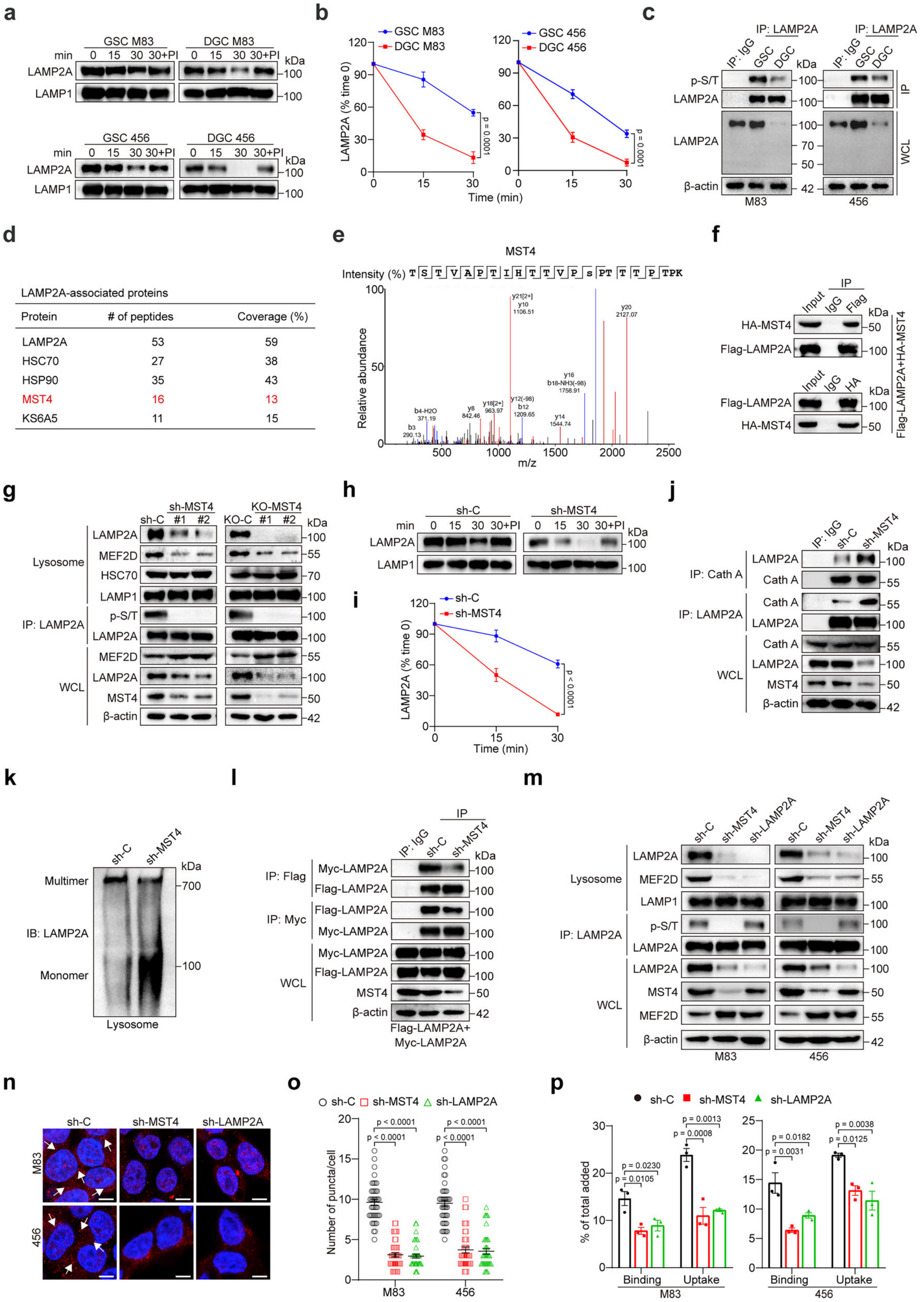

Protein	# of peptides	Coverage (%)
LAMP2A	53	59
HSC70	27	38
HSP90	35	43
MST4	16	13
KS6A5	11	15

aforementioned findings demonstrated no significant discrepancies in the mRNA level of *LAMP2A* between GSC and DGC cell lines (Supplementary Fig. 1b), suggesting an absence of differential de novo protein synthesis. In contrast, assessments of lysosomal LAMP2A stability over different incubation time in an isotonic buffer demonstrated that the degradation of LAMP2A was significantly accelerated in lysosomes derived from DGCs compared to their GSCs counterparts (Fig. 2a, b). The observed alterations in DGCs were markedly reversed when lysosomes were treated with protease inhibitor cocktail (PI), which block lysosomal proteolytic activity and thereby prevent LAMP2A luminal degradation[21]. This suggests that the reduced stability of LAMP2A is mainly caused by increased lysosomal degradation (Fig. 2a). To elucidate the mechanisms governing lysosomal LAMP2A stability in GSCs, we conducted an analysis of the post-translational modifications

Fig. 2 | MST4 enhances the lysosomal abundance of the CMA regulator LAMP2A. Assessment of LAMP2A stability in lysosomes isolated from indicated GSCs and DGCs (**a**), as well as GSC M83 cells expressing sh-C or sh-MST4 (**h**). Lysosomes were incubated at 0 °C for 10 min with or without protease inhibitor cocktail (PI) to inhibit lysosomal protease activity, followed by pelleting at indicated time points, and subsequent IB analysis for LAMP2A and LAMP1 densitometric quantification. **b, i** Densitometric quantification of LAMP2A protein level is shown. $n = 3$ independent experiments. **c** IP-IB analyses for indicated proteins in GSCs and DGCs. WCL, whole-cell lysates. Immunoglobulin G (IgG) was used as an isotype control. **d** A list of top LAMP2A-associated proteins identified through LAMP2A immunoprecipitation and mass spectrometric analysis. We marked the protein of interest in red font. **e** Identification of MST4 peptide among LAMP2A-interacting proteins precipitated from GSCs via mass spectrometry. y-ions generated from C-terminal (red), b-ions generated from N-terminal (blue), other fragments (black). **f, j, l** IP-IB analyses in GSC M83 cells with indicated modifications. **g, m** IP-IB analyses for indicated proteins in WCL and lysosomal fractions of GSCs with indicated modifications. β-actin and LAMP1 served as loading controls for WCL and lysosomal samples, respectively. **k** Purified lysosomal membranes from the indicated GSC M83 cells were analyzed using native continuous gel electrophoresis and subjected to IB detection for LAMP2A. **n, o** Representative images (**n**) and quantification (**o**) of CMA activity detection by KFERQ puncta numbers in GSC M83 and 456 cells with indicated modifications. $n = 40$ randomly selected cells. Scale bar, 10 µm. **p** In vitro binding and uptake assay of GAPDH by the lysosome in GSC M83 and 456 cells with indicated modifications. Protease inhibitor cocktail (PI) was used to inhibit lysosomal protease activity. $n = 3$ independent experiments. Data are presented as the means ± S.E.M. All the experiments showed consistent results in at least three independent biological replicates. Statistical significance was assessed using two-way ANOVA with Bonferroni's multiple comparisons test (**b, i**) or one-way ANOVA with Dunnett's multiple comparisons test (**o, p**). Source data are provided as a Source Data file.

of LAMP2A proteins in both GSCs and DGCs. Previous studies have indicated that glycosylation plays a role in the regulated stability of LAMP2A[41]. To assess the glycosylation status of LAMP2A, we performed both PNGase F deglycosylation and Concanavalin A (ConA) lectin blotting analyses. Enzymatic deglycosylation resulted in a consistent molecular weight shift of LAMP2A monomers from ~100 kDa to ~50 kDa in both GSCs and DGCs, demonstrating complete N-linked glycan removal. This identical migration pattern strongly suggests equivalent glycosylation profiles between the two cell types. Supporting this conclusion, ConA blotting analysis confirmed comparable glycosylation levels in GSCs and DGCs (Supplementary Fig. 2a). In contrast, we observed that GSCs exhibited elevated level of LAMP2A phosphorylation compared to DGCs (Fig. 2c).

To determine if LAMP2A phosphorylation is necessary for its stability in GSC lysosomes, we performed a proteomic analysis of kinase proteins that co-precipitated with LAMP2A in GSCs (Supplementary Fig. 2b). Among the top associated proteins, we identified MST4 is associated with LAMP2A, subsequently confirming their interaction through reciprocal immunoprecipitation (Fig. 2d, f and Supplementary Fig. 2c). Immunofluorescence analysis also revealed that MST4 co-localized with LAMP2A in GSC M83 and 456 cells (Supplementary Fig. 2d). Characterization of the interaction domains between MST4 and LAMP2A indicated that the N-terminal region (amino acids 1-137) of LAMP2A, alongside the kinase domain of MST4 (amino acids 1-279), is essential for their interaction (Supplementary Fig. 2e–h). CMA has been identified as a component of the cellular adaptive mechanisms to stress[10,16,42]. We examined the effects of irradiation (IR) and nutrient deprivation on the interaction between MST4 and LAMP2A. Our results indicated that IR significantly increased MST4 expression and enhanced the interaction between MST4 and LAMP2A (Supplementary Fig. 2i). While growth factors (EGF/FGF) deprivation did not influence the interaction between MST4 and LAMP2A (Supplementary Fig. 2j), culturing them in serum-supplemented medium diminished the MST4-LAMP2A interaction (Supplementary Fig. 2k). Collectively, these results suggest that targeting the MST4-LAMP2A axis may sensitize GSCs to microenvironmental stresses, such as hypoxia and nutrient limitation, thereby providing a potential therapeutic strategy to eliminate therapy-resistant GSCs.

To investigate the role of MST4 in CMA within GSCs, we conducted MST4 KD via shRNAs and knockout (KO) utilizing single guide RNAs (sgRNAs). Notably, the phosphorylation level of LAMP2A and the lysosomal presence of LAMP2A were significantly diminished following MST4 deletion (Fig. 2g). Given that the proper localization of LAMP2A at the lysosome, along with its molecular multimerization and interaction with lysosomal proteases, governs its stability and functionality[10], we sought to elucidate the underlying mechanisms responsible for the observed decline in lysosomal LAMP2A in the absence of MST4 expression. We found that there were no significant differences in *LAMP2A* mRNA level between MST4-KD GSCs and control cells (Supplementary Fig. 2l). Subsequently, we hypothesized that MST4 might be essential for the localization of LAMP2A. Examination of LAMP2A's subcellular localization indicated that its presence at lysosomal structures remained unaffected by the absence of MST4 (Supplementary Fig. 2m), implying that MST4 is not critical for the proper subcellular distribution of LAMP2A. We then posited that MST4 loss could compromise the stability of LAMP2A at the lysosome. To evaluate this hypothesis, we assessed the stability of LAMP2A in GSCs. The KD of MST4 resulted in a more rapid degradation of LAMP2A, which was significantly mitigated when MST4-KD GSCs exposed to lysosomal PI (Fig. 2h, i), indicating that the diminished stability of LAMP2A following MST4 deletion was primarily due to enhanced degradation within lysosomal compartments. The targeted cleavage of LAMP2A by Cathepsin A (Cath A) at the lysosomal membrane serves as the catalyst for its degradation within the lysosomal environment[43]. Our findings demonstrated that MST4 KD was associated with an increased interaction of LAMP2A with Cath A (Fig. 2j), corroborating the elevated degradation rate of LAMP2A following MST4 KD. Furthermore, native electrophoresis analysis of LAMP2A's multimeric status at the lysosomal membrane exhibited a substantial decrease in the formation of the 700 kDa multimeric complex necessary for substrate translocation in lysosomes from MST4-KD GSCs (Fig. 2k). These results aligned with the observed reduction in the interaction among LAMP2A molecules in MST4-KD GSCs (Fig. 2l). Collectively, these findings underscored the role of MST4 in facilitating LAMP2A stability in the lysosomes and its active conformational dynamics.

Changes in the abundance of lysosomal LAMP2A have been found to influence CMA activity[13]. Knocking down endogenous MST4 or LAMP2A with specific shRNAs in GSC M83 and 456 cells led to reduced level of phosphorylated LAMP2A. This change led to an increase in MEF2D within the whole cellular lysate while reducing its presence in the lysosomal fraction, a decrease in KFERQ-puncta, and impaired lysosomal binding and uptake of the CMA substrate GAPDH (Fig. 2m-p). To further explore the role of MST4 in inducing CMA, we overexpressed exogenous MST4-WT and kinase-dead mutants (T178A and K53E) in GSC 23 cells with low endogenous MST4 level. The overexpression of WT MST4, unlike the kinase-dead mutants, led to increased phosphorylation of LAMP2A, reduced interaction between LAMP2A and Cath A, higher accumulation of LAMP2A in lysosomes, and enhanced CMA activity in GSCs (Supplementary Fig. 2n, o).

MST4 directly phosphorylates LAMP2A in GSCs

Based on the interaction between MST4 and LAMP2A, as well as the role of MST4 in CMA, we investigated whether MST4 phosphorylates LAMP2A and affects its stability. To identify the phosphorylation sites on LAMP2A by MST4, we conducted mass spectrometry on Flag-LAMP2A from HEK293T cells that stably overexpress exogenous HA-MST4 and Flag-LAMP2A. Our findings indicated that the residues T40,

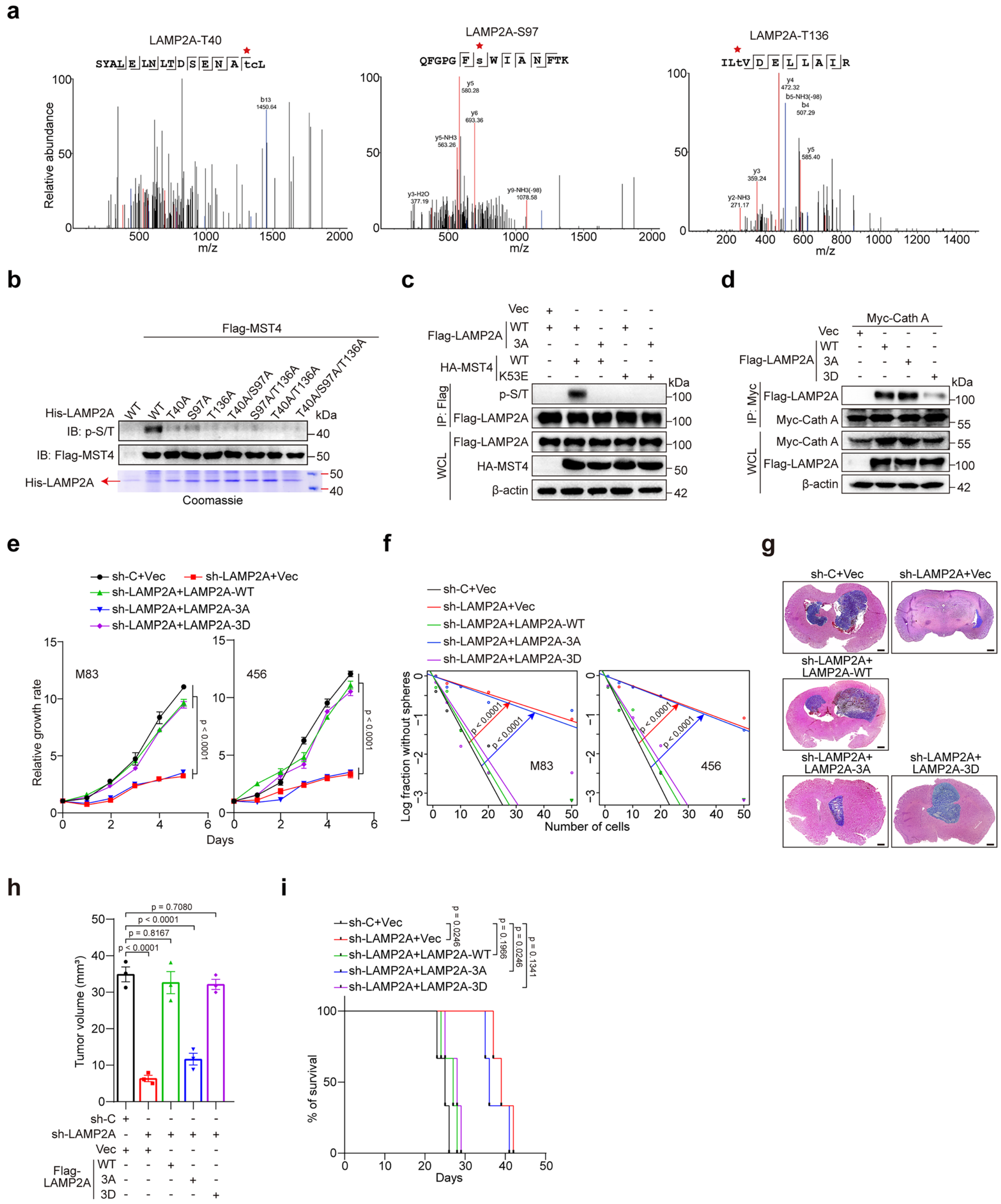

S97, and T136 of LAMP2A underwent specific phosphorylation in cells that express exogenous MST4, in contrast to those transfected with a control vector (Fig. 3a). The amino acid sequences surrounding T40, S97, and T136 are highly conserved in LAMP2A among multiple species (Supplementary Fig. 3a). To identify the key phosphorylation site(s) of LAMP2A influenced by MST4, we individually or in combination mutated the serine/threonine residues at T40, S97, and T136 to alanine. The in vitro kinase assay revealed that wild-type LAMP2A was phosphorylated by MST4. Mutating each site alone slightly reduced phosphorylation, while mutating any two sites significantly decreased it, and mutating all the three sites completely abrogated phosphorylation. Among the three single-site mutations, the T136 mutation showed the most significant reduction in phosphorylation level, indicating that T136 site is crucial for LAMP2A phosphorylation (Fig. 3b). Additionally, we co-expressed WT LAMP2A or T40A/S97A/T136A (3 A) mutant and MST4-WT or -K53E in HEK293T cells, the result identified phosphorylation in WT LAMP2A, but not in the non-phosphorylatable 3 A mutant or kinase dead mutant K53E (Fig. 3c). To validate our

Fig. 3 | MST4 phosphorylates LAMP2A through direct interaction. a Mass-spectrometric analysis of p-LAMP2A in HEK293T cells co-overexpressing Flag-LAMP2A and HA-MST4. Asterisk at the top, threonine 40, serine 97 and threonine 136 residues that were found phosphorylated determined by mass spectrometric analysis. y-ions generated from C-terminal (red), b-ions generated from N-terminal (blue), other fragments (black). **b** In vitro kinase assays utilizing wild-type (WT) MST4 with either LAMP2A-WT or indicated mutants as substrates, followed by SDS-PAGE analysis and IB detection with an anti-Flag antibody, anti-p-S/T antibody and veriBlot for IP Detection Reagent (HRP). **c** IP-IB analyses for the indicated proteins in HEK293T cells transduced with the indicated plasmids. **d** IP-IB analyses for the indicated proteins in GSC M83 cells expressing Myc-Cath A along with Flag-LAMP2A-WT or indicated mutants. **e, f** Cell proliferation (**e**) and sphere-forming frequency (**f**) of GSC M83 and 456 cells with indicated modifications. $n = 3$ independent experiments in (**e**). **g, h** Representative H&E images mouse brain sections (**g**) and quantitative analysis of tumor volume (**h**) from athymic (BALB/c Nude) mice intracranially implanted with GSC M83 cells with indicated modifications. $n = 3$ mice per group. Scale bar, 1.0 mm. **i** Kaplan-Meier survival curves of athymic (BALB/c Nude) mice intracranially transplanted with GSC M83 cells with indicated modifications. $n = 3$ mice per group. Data are presented as the means ± S.E.M. All the experiments showed consistent results in at least three independent biological replicates. Statistical significance was assessed using one-way ANOVA with Tukey's multiple comparisons test (**e**), two-sided likelihood ratio test (**f**), one-way ANOVA with Dunnett's multiple comparisons test (**h**) or log-rank test (**i**). ns, not significant. Source data are provided as a Source Data file.

findings, we developed a murine antibody that specifically targets the T136 phosphorylated LAMP2A peptide, without reacting to the non-phosphorylated version (Supplementary Fig. 3b). This antibody, known as the p-LAMP2A antibody, effectively detected T136 phosphorylation of endogenous LAMP2A. In GSC M83 cells, KD or KO of MST4 significantly reduced the level of phosphorylated LAMP2A at T136 (Supplementary Fig. 3c). In HEK293T cells co-expressing HA-MST4 and Flag-LAMP2A, the p-LAMP2A antibody specifically detected phosphorylation in LAMP2A-WT, T40A, S97A, and T40A/S97A under exogenous overexpression conditions. However, it completely failed to recognize the T136A phospho-null mutant (T136A), as well as all mutants containing the T136A substitution (T136A/T40A, T136A/S97A, and 3 A) (Supplementary Fig. 3d). Moreover, the p-LAMP2A antibody was employed to observe pT136 levels in exogenous LAMP2A-WT and −3A within GSC M83 cells. The p-LAMP2A signal was exclusively detected in GSCs expressing LAMP2A-WT, with no signal observed for LAMP2A-3A (Supplementary Fig. 3e).

To assess the role of LAMP2A phosphorylation in CMA activation, we knocked down endogenous LAMP2A in GSCs using specific shRNA and then reintroduced shRNA-resistant LAMP2A-WT, −3A, or phosphorylation-mimic −3D mutant. The findings indicated that both WT and 3D variants effectively reconstituted lysosomal LAMP2A levels and restored CMA-mediated MEF2D degradation capacity, while the 3 A mutant failed to do so (Supplementary Fig. 3f). Additionally, LAMP2A-3A significantly impaired LAMP2A oligomerization compared to LAMP2A-WT (Supplementary Fig. 3g). Coimmunoprecipitation analyses further revealed that LAMP2A-3A attenuated homotypic LAMP2A-3A interactions relative to WT or 3D variants (Supplementary Fig. 3h). Moreover, LAMP2A-3D mutant displayed reduced binding affinity for Cath A while simultaneously enhancing KFERQ-positive puncta formation (Fig. 3d and Supplementary Fig. 3i, j). Additionally, LAMP2A-WT and −3D, but not −3A mutant, successfully rescued GSC cell proliferation and sphere formation in vitro (Fig. 3e, f), and tumorigenicity, which resulted in a shorter survival time of GSC-bearing mice (Fig. 3g–i).

To determine if the increased stability of phosphorylated LAMP2A at the lysosomal membrane is a common mechanism across different cell types, we analyzed human MRC-5 fibroblasts. We compared the half-life and phosphorylation levels of LAMP2A in lysosomal membranes of early-passage (P18) and late-passage (P45) fibroblasts. Late-passage fibroblasts showed a significantly faster degradation rate of LAMP2A (Supplementary Fig. 4a, b) and had lower levels of phosphorylated LAMP2A (Supplementary Fig. 4c) compared to early-passage cells. To investigate whether enhancing LAMP2A phosphorylation could rescue CMA dysfunction in aging-like models, we introduced LAMP2A-WT, −3A, or −3D into MRC-5 fibroblasts. Notably, LAMP2A-WT and −3D significantly decreased the number of senescence-associated beta-galactosidase (SA-β-gal) positive cells in late-passage fibroblasts, while −3A did not (Supplementary Fig. 4d). This improvement correlated with a decrease in known CMA substrates (MEF2D and GAPDH) in whole-cell lysates and their accumulation in lysosomal fractions (Supplementary Fig. 4e, f), indicating enhanced degradation through CMA. These findings suggest that the phosphorylation-dependent stabilization of LAMP2A is a conserved mechanism across cell types, and that mimicking phosphorylation (LAMP2A-3D) can improve CMA dysfunction in aging-like models.

MST4-mediated phosphorylation of LAMP2A promotes CMA activity, self-renewal, and tumorigenicity of GSCs

To further assess the importance of MST4-mediated LAMP2A phosphorylation in CMA activity and GSC biological function, we reintroduced the LAMP2A-WT or −3D mutant into GSC M83 and 456 cells, where endogenous MST4 expression was downregulated using shRNA (Supplementary Fig. 5a). Western blot analysis of lysosomal fractions from these control cells showed a significant accumulation of lysosomal proteins (LAMP1, LAMP2A, and HSC70) and an increase in phosphorylated LAMP2A compared to whole cell lysates, indicating functional CMA in the lysosomes (Fig. 4a and Supplementary Fig. 5b). Absence of mitochondrial (COX IV) and cytosolic (β-actin) markers in the lysosomal samples confirmed their purity (Fig. 4a and Supplementary Fig. 5b). Our findings revealed that the CMA-competent lysosomes exhibited reduced levels of phosphorylated and total LAMP2A when endogenous MST4 was deleted in GSC M83 and 456 cells (Fig. 4a and Supplementary Fig. 5b). In contrast, the introduction of the exogenous phosphomimetic LAMP2A-3D, in contrast to LAMP2A-WT, significantly reinstated the level of lysosomal LAMP2A (Fig. 4a), enhanced the number of KFERQ puncta (Fig. 4b and Supplementary Fig. 5c, d), and improved the binding and uptake of GAPDH within lysosomes that were diminished due to MST4 KD (Fig. 4c). Additionally, LAMP2A-3D, but not -WT, notably enhanced the proliferation and sphere-forming capacity of GSC M83 and 456 cells in vitro (Fig. 4d, e). In vivo investigations revealed that LAMP2A-3D, in contrast to the LAMP2A-WT, markedly restored the tumorigenic capacity of orthotopic GSC xenografts (Fig. 4f, g) and significantly reduced the survival duration of the animals (Fig. 4h).

In GSC 23 cells devoid of detectable MST4, the introduction of exogenous MST4 resulted in elevated levels of both phosphorylated and total LAMP2A within CMA-active lysosomes, as well as an increased association of MEF2D with lysosomes (Fig. 4i and Supplementary Fig. 5e). Additionally, overexpression of MST4 augmented CMA activity, evidenced by the higher abundance of KFERQ puncta (Fig. 4j, k), and enhanced lysosomal binding and uptake of GAPDH (Fig. 4l). Conversely, silencing of endogenous LAMP2A abrogated the stimulatory effects of MST4 overexpression on CMA activity (Fig. 4j–l). Moreover, MST4 promoted the proliferation and sphere-forming capacity of GSC cells in vitro (Fig. 4m, n), along with enhancing tumorigenicity in vivo (Fig. 4o–q). However, knockdown of endogenous LAMP2A markedly inhibited cell growth and reduced the frequency of sphere formation in GSC 23 cells (Fig. 4m, n), while also decelerating MST4-mediated tumor growth in xenograft models, ultimately leading to improved survival outcomes in the animal subjects (Fig. 4o–q). Interestingly, GSC 23 cells exhibited elevated levels of LAMP2A phosphorylation, although not at the T136 site (Supplementary Fig. 5f). When treated with SB203580, a p38α MAPK inhibitor[44],

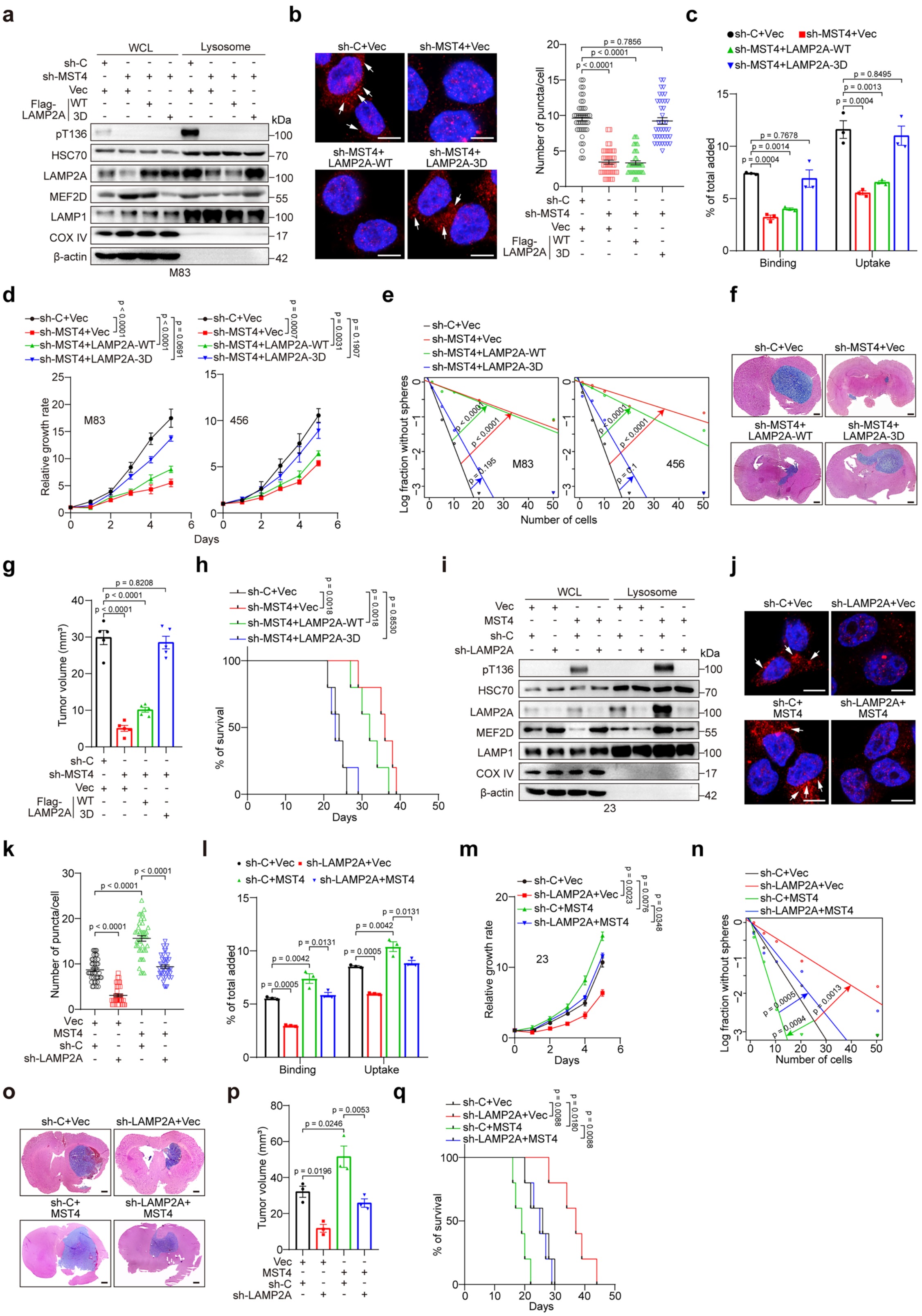

there was a decrease in phosphorylated LAMP2A and lysosomal LAMP2A, along with reduced MEF2D association with lysosomes, leading to increased MEF2D accumulation in the total cell lysate (Supplementary Fig. 5g). This indicates that the phosphorylation of LAMP2A mediated by p38α MAPK is vital for maintaining basal CMA activity within GSC 23 cells. Furthermore, we observed that MST4 activates both macroautophagy and CMA in GSCs, with these pathways exhibiting compensatory interactions (Supplementary Fig. 6a–c). In xenograft models, the knockdown of either ATG4B or LAMP2A led to a reduction in MST4-driven tumor growth by 73% and 68% ($p < 0.001$), respectively (Supplementary Fig. 6d, e). Notably, the combined inhibition of ATG4B and LAMP2A synergistically decreased tumor burden by 97% ($p < 0.001$) and extended median survival from 16 days (MST4 overexpression) to 45 days ($p < 0.01$) (Supplementary Fig. 6f).

Fig. 4 | MST4-mediated phosphorylation of LAMP2A maintains CMA activity and GSC properties. a, i IB analyses for indicated proteins in WCL and lysosomal fractions of GSC M83 cells (**a**) or GSC 23 cells (**i**) with indicated modifications. Representative images (left in **b**, or **j**) and quantification (right in **b**, or **k**) of CMA activity detection by KFERQ puncta numbers in GSC M83 cells (**b**) or GSC 23 cells (**j**-**k**) with indicated modifications. *n* = 40 randomly selected cells. Scale bar, 10 µm. **c, l** In vitro binding and uptake assay of GAPDH by the lysosome in GSC M83 cells (**c**) or GSC 23 cells (**l**) with indicated modifications. *n* = 3 independent experiments. **d-e, m-n** Cell proliferation (**d, m**) and sphere-forming frequency (**e, n**) of GSC M83 and 456 cells (**d-e**) and GSC 23 cells (**m-n**) with indicated modifications. *n* = 3 independent experiments. **f, g** Representative H&E images of mouse brain sections (**f**) and quantitative analysis of tumor volume (**g**) from athymic (BALB/c Nude) mice intracranially implanted with GSC M83 cells with indicated modifications. *n* = 5 mice per group. Scale bar, 1.0 mm. **h** Kaplan-Meier survival curves of athymic (BALB/c Nude) mice intracranially transplanted with GSC M83 cells with indicated modifications. *n* = 5 mice per group. **o, p** Representative H&E images of mouse brain sections (**o**) and quantitative analysis of tumor volume (**p**) from athymic (BALB/c Nude) mice intracranially implanted with GSC 23 cells with indicated modifications. *n* = 3 mice per group. Scale bar, 1.0 mm. **q** Kaplan-Meier survival curves of athymic (BALB/c Nude) mice intracranially transplanted with GSC 23 cells with indicated modifications. *n* = 5 mice per group. Data are presented as the means ± S.E.M. All the experiments showed consistent results in at least three independent biological replicates. Statistical significance was assessed using one-way ANOVA with Dunnett's multiple comparisons test (**b, c, d, g**), two-sided likelihood ratio test (**e, n**), log-rank test (**h, q**) or one-way ANOVA with Tukey's multiple comparisons test (**k, l, m, p**). ns, not significant. Source data are provided as a Source Data file.

Consistent with the above observation, immunostaining revealed identical distribution patterns for both LAMP2A and LC3B (Supplementary Fig. 6g-i).

CMA acts as an enhancer of mTORC1 signaling by modulating TSC1/2

To elucidate the pathways potentially modulated by CMA in GSCs, we queried previously published RNA-seq data (GSE181556) and proteomics data (PXD027069) from patient-derived GSCs with and without LAMP2A deletion[17]. Gene set enrichment analysis (GSEA) of RNA-seq data indicated that LAMP2A KD resulted in an upregulation of interferon response and other inflammation-associated genes, while concurrently downregulating the PI3K-AKT-mTOR signaling cascade (Fig. 5a). The proteomic investigation underscored the STING-mediated activation of host immune responses, interferon signaling, and translation as the primary pathways exhibiting significant alterations (Fig. 5b).

The mTORC1 activity is frequently dysregulated in various human cancers, including GBM[45]. The constitutive activation of mTORC1 is essential for the proliferation, self-renewal, and tumorigenic potential of cancer stem cells[46–48]. Given that the interplay between CMA and mTORC1 signaling had not been previously explored, we subsequently investigated whether CMA influences mTORC1 activity. mTORC1 has two extensively studied substrates, ribosomal protein S6 kinase (P70S6K) and eukaryotic translation initiation factor 4E-binding protein 1 (4EBP1), which play essential roles in the regulation of protein biosynthesis[49]. KD of MST4 or LAMP2A led to a marked reduction in the phosphorylation levels of P70S6K and 4EBP1 (Fig. 5c), indicating that CMA regulates mTORC1 activity.

Subsequently, we examined whether CMA was required for the targeted degradation of mTOR signaling inhibitors. CMA is a specialized autophagic process characterized by substrate specificity determined by the presence of a pentapeptide motif resembling KFERQ within the substrate protein, enabling recognition by cytosolic HSC70[10]. We screened for mTORC1-upstream proteins that were upregulated after LAMP2A KD in GSCs and had motifs in their amino acid sequences making them susceptible to CMA. Notably, we detected such motifs in tuberous sclerosis complex 1 (TSC1) and 2 (TSC2), which are recognized as critical upstream negative regulators of mTORC1[50]. We compared the motifs and found that both TSC1 and TSC2 possess the KFERQ-like motif (Supplementary Table 1). Additionally, we confirmed that HSC70 and LAMP2A bind to WT TSC1/2, but not to TSC1/2 mutants (Supplementary Table 1) with altered HSC70 binding motifs (Fig. 5d, e), which displayed a longer half-life than their WT counterparts (Fig. 5f, g). Furthermore, the depletion of HSC70 or LAMP2A resulted in a reduced association of TSC1/2 with lysosomal compartments, and subsequently led to an increased expression of TSC1/2 in GSCs (Fig. 5h, i). Conversely, the overexpression of LAMP2A-WT or −3D, as opposed to −3A or −4A, markedly decreased the protein levels of TSC1/2 in HEK293T cells (Supplementary Fig. 7a). Immunofluorescence staining illustrated that TSC1/2 co-localized with LAMP2A-positive lysosomes under conditions that induce CMA, such as nutrient starvation. This association with lysosomes was disrupted when the KFERQ motifs were mutated (Supplementary Fig. 7b, c). Finally, we conducted in vitro uptake assays utilizing lysosomes isolated from HEK293T cells that were active in CMA. Purified TSC1/2 proteins were incubated with either untreated lysosomes or those that had been pretreated with lysosomal PI. Immunoblotting of the recovered lysosomes demonstrated the uptake and degradation of TSC1/2 by these lysosomes (Supplementary Fig. 7d, e). Together, these findings indicate that TSC1/2 are indeed targets of CMA.

To investigate the degradation of TSC1/2 proteins within lysosomes, we quantified the levels of lysosomal TSC1/2 in GSCs with and without cycloheximide (CHX). The application of LN, which inhibit lysosomal proteolysis, resulted in a significant elevation of TSC1/2 levels, comparable to those observed following proteasome inhibition previously linked to TSC1/2 degradation (Fig. 5j). Conversely, the suppression of macroautophagy using 3-MA did not alter the intracellular concentrations of TSC1/2, indicating that a portion of TSC1/2 undergoes routine degradation in lysosomes (Fig. 5j). Additionally, KD of TSC1/2 substantially mitigated the effects of LAMP2A KD on mTORC1 pathway activity (Supplementary Fig. 8a), GSC cell growth (Supplementary Fig. 8b), and sphere-forming frequency (Supplementary Fig. 8c, d). To further elucidate the role of CMA in TSC1/2 degradation and its impact on GSC tumorigenicity, we performed KD of endogenous TSC1/2 protein levels, followed by the reintroduction of shRNA-resistant TSC1/2 wild-type and HSC70 binding motif-mutated variants (Supplementary Fig. 8e). The KD of TSC1/2 enhanced GSC proliferation and spheroid formation, whereas the re-expression of exogenous TSC1/2 WT fully rescued the effects of TSC1/2 deficiency on mTOR activity and GSC phenotypes (Fig. 5k, l and Supplementary Fig. 8f, g). Intriguingly, the reintroduction of TSC1/2 mutants exerted even stronger effects than WT, suggesting that these mutants escape endogenous CMA-mediated suppression, thereby exerting enhanced effects on downstream mTOR signaling and GSC phenotypes (Fig. 5k, l and Supplementary Fig. 8f, g). Under standard culture conditions, the genetic knockdown or reconstitution of TSC1/2 expression markedly influenced mTORC1 signaling, while exhibiting no significant impact on the macroautophagic flux, as determined by quantitative assessment of the LC3-II/I ratio and levels of p62 protein (Supplementary Fig. 8h). This observation was corroborated by the absence of substantial alterations in LC3B puncta formation in tumor tissues modified for TSC1/2 expression compared to control samples. Importantly, ATG5 knockdown, employed as a positive control for macroautophagy inhibition, consistently demonstrated the anticipated impairment of macroautophagy both in vitro and in vivo (Supplementary Fig. 8h-j). In summary, these findings indicated that CMA facilitates GSC proliferation, self-renewal, and tumorigenicity through mTORC1 activation via the lysosomal degradation of TSC1/2, rather than through modifications in macroautophagy levels.

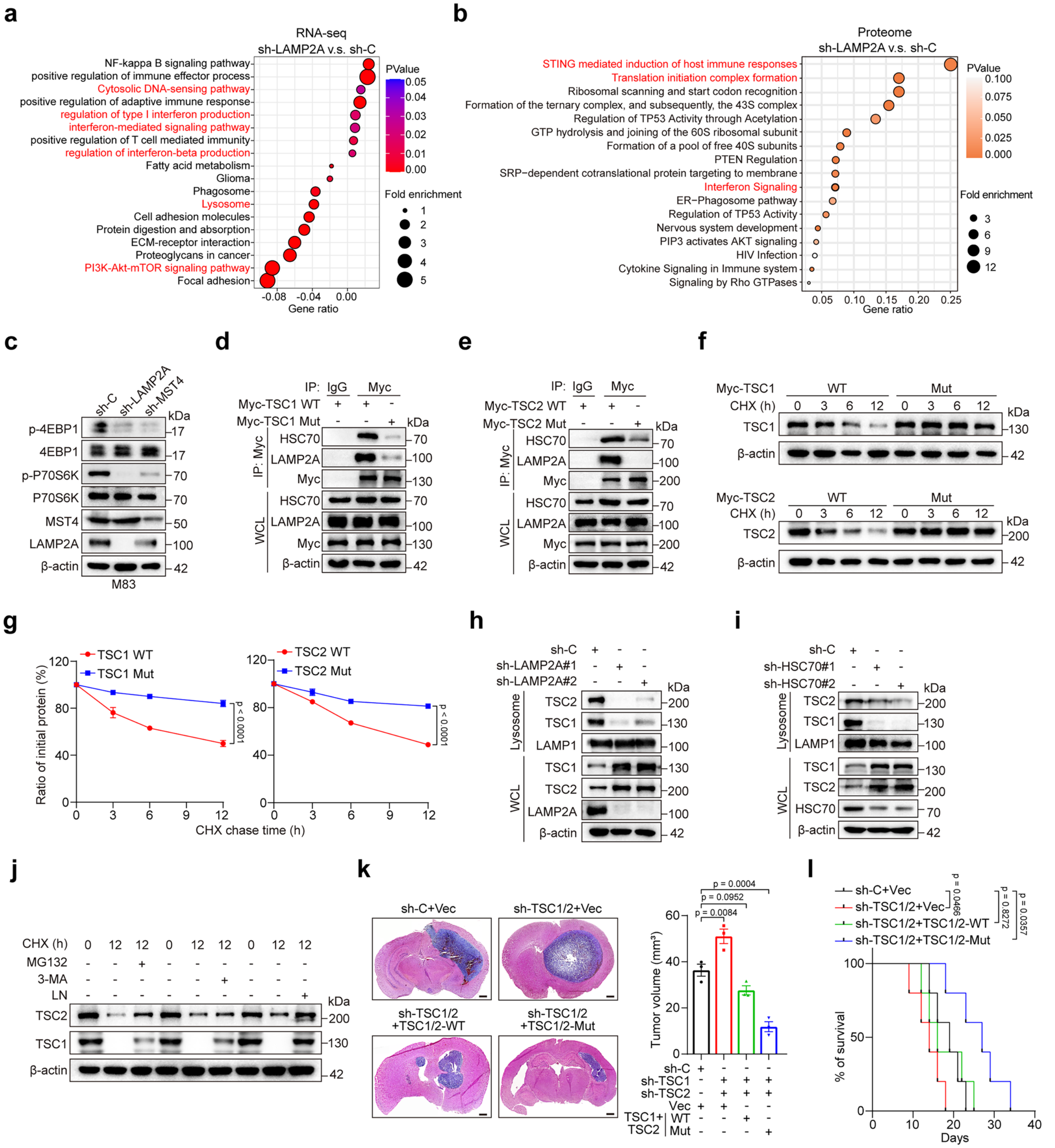

Fig. 5 | CMA regulates mTORC1 activity through lysosomal degradation of TSC1/2. a, b Gene set enrichment analysis highlighted the main biological processes significantly altered due to LAMP2A KD in GSCs, derived from RNA-seq data (GSE181556, **a**) and proteomic data (PXD027069, **b**). These pathways of interest especially immune-related pathways are indicated in red. **c** IB analyses for indicated proteins in GSC M83 cells expressing sh-C, sh-MST4 or sh-LAMP2A. **d, e** IP-IB analyses for indicated proteins in HEK293T cells transduced with the indicated plasmids. **f** IB for TSC1 (top) and TSC2 (bottom) in HEK293T cells subjected to indicated modifications, subsequently treated with CHX (100 μg/mL) for the indicated time. **g** Quantification of TSC1 (left) and TSC2 (right) protein levels in HEK293T cells with indicated modifications and treatments. $n = 3$ independent experiments. **h, i** IB analyses for TSC1/2 protein levels in WCL and lysosomal fractions of GSC M83 cells, with or without LAMP2A KD (**h**) or HSC70 KD (**i**). **j** IB analyses for TSC1 and TSC2 in GSC M83 cells, either untreated or subjected to 10 μM MG132, 5 mM 3-MA or LN (10 μM leupeptin and 20 mM NH_4Cl) for an additional 12 hours post-CHX (100 μg/mL) treatment for 12 h. **k** Representative H&E images of mouse brain sections (left) and quantification of tumor volume (right) from athymic (BALB/c Nude) mice intracranially implanted with GSC M83 cells with indicated modifications. $n = 3$ mice per group. Scale bar, 1.0 mm. **l** Kaplan-Meier survival curves of athymic (BALB/c Nude) mice intracranially transplanted with GSC M83 cells with indicated modifications. $n = 5$ mice per group. Data are presented as the means ± S.E.M. All the experiments showed consistent results in at least three independent biological replicates. Statistical significance was assessed using one-sided Fisher's exact test (**a, b**), two-way ANOVA with Bonferroni's multiple comparisons test (**g**), one-way ANOVA with Dunnett's multiple comparisons test (**k**) or log-rank test (**l**). ns, not significant. Source data are provided as a Source Data file.

Inhibiting CMA function reduces GBM tumor growth by enhancing anti-tumor T cell immunity

Our findings indicated an enrichment of interferon response genes and an inflammatory gene signature in GSCs with LAMP2A KD (Fig. 5a, b), prompting us to explore the impact of targeting the MST4-LAMP2A-CMA pathway on host anti-tumor immunity. To evaluate the influence of CMA on the immune microenvironment, we adopted the CMA score as recently established by Bourdenx et al. [51] This score serves as a weighted average of the expression levels of all known effectors, as well as both positive and negative regulators of CMA, with recent research indicating that it serves as a reliable metric for assessing CMA activation status[19,52]. TCGA analysis revealed that CMA score negatively correlated with CD8$^+$ T cell infiltration and positively correlated with tumor-associated macrophages (TAMs) and myeloid-derived suppressor cells (MDSCs) in GBM. There was no significant correlation with regulatory T cells (Tregs) (Fig. 6a and Supplementary Fig. 9a-e). Additionally, we conducted in vitro co-cultures of GSCs with MST4 or LAMP2A KD alongside allogeneic human CD8$^+$ T cells. Flow cytometric analysis indicated that the KD of LAMP2A or MST4 significantly enhanced cytotoxic T cell activity, evidenced by increased production of polyfunctional cytokines such as TNF-α (Fig. 6b) and IFN-γ (Fig. 6c), elevated effector degranulation (Granzyme B, GZMB) (Fig. 6d), and increased apoptosis in GSCs (Supplementary Fig. 9f).

Due to the inability of GSCs to engraft in immunocompetent C57BL/6 mice because of species-specific barriers, we performed KD of endogenous Mst4 or Lamp2a in murine syngeneic GBM cell lines, GL261 and CT-2A (Fig. 6e), and subsequently implanted $1×10^5$ viable GL261 cells intracranially into immunodeficient BALB/c Nude mice or immunocompetent C57BL/6 mice. Compared to the control cohort, the ablation of Mst4 or Lamp2a in murine GBM cells resulted in a moderate yet significant reduction in intracranial tumor growth in immunodeficient nude mice, as evidenced by bioluminescence imaging and H&E staining of tumor progression, and survival analysis (Fig. 6f–j). Notably, the deletion of Mst4 or Lamp2a produced a pronounced anti-tumor response in C57BL/6 mice, compared to BALB/c Nude mice, leading to an extension of overall survival (Fig. 6f–k), underscoring the pivotal role of T cell-mediated immune surveillance in tumor inhibition. Immunofluorescence examination of murine tissues indicated that the absence of Mst4 and Lamp2a resulted in a reduction of PD-L1 expression and a decrease in the infiltration of immunosuppressive Tregs (Supplementary Fig. 9g, h), while simultaneously promoting the infiltration and cytotoxic activity of CD8$^+$ T cells within the xenograft tumors, evidenced by the enhanced co-localization of CD8 and GZMB (Supplementary Fig. 9i). Consistent with the immunofluorescence data, flow cytometric analysis revealed a notable increase in the presence of functionally active CD8$^+$ T cells and a reduction in Treg infiltration in tumors following the deletion of Mst4 or Lamp2a (Supplementary Fig. 9j–m). Additionally, Mst4 KD reduced tumor infiltration of immunosuppressive cells (Tregs, TAMs, and MDSCs). However, re-expressing LAMP2A-WT or −3D significantly restored the reduction in immunosuppressive cell infiltration (Supplementary Fig. 9n–p). These findings underscore the involvement of CMA in the formation of the immunosuppressive microenvironment characteristic of GBM.

To ascertain whether the tumor growth inhibition associated with LAMP2A depletion was mediated by anti-tumor CD8$^+$ T cell immunity, CT-2A GBM-bearing mice were administered an anti-CD8α monoclonal antibody (mAb). In contrast to the IgG2b control mAb, the administration of the CD8α mAb markedly reversed the tumor growth inhibitory effects of Lamp2a depletion and correspondingly decreased the survival of GBM-bearing mice (34 d in sh-Lamp2a plus IgG2b versus 24.5 d in sh-Lamp2a plus CD8α mAb, Fig. 6l–n). Collectively, these findings implied that the inhibition of CMA attenuates GBM tumorigenesis by facilitating CD8$^+$ T cell infiltration and enhancing cytotoxic activity.

CMA regulates cGAS/STING expression through targeting TET3 for lysosomal degradation

The cyclic GMP-AMP synthase (cGAS)-stimulator of interferon genes (STING) pathway has been identified as a pivotal mechanism in anti-tumor immunity, regulating the production of interferons and pro-inflammatory cytokines in response to cytosolic DNA or DNA damage[53]. Given the above results (Fig. 5b), further analysis also showed that LAMP2A KD altered the STING-mediated immune response and interferon signaling (Fig. 7a, b). Subsequently, we investigated whether the MST4-LAMP2A signaling axis influences cGAS-STING signaling. The ablation of either MST4 or LAMP2A resulted in an upregulation of cGAS and STING at both the protein and mRNA levels, which was accompanied by enhanced phosphorylation of TBK1 and STING upon IR stimulation (Fig. 7c–f). Collectively, these results implied that the MST4-LAMP2A signaling pathway modulates cGAS-STING activation by affecting the transcriptional regulation of cGAS and STING.

Promoter regions of *CGAS* and *STING* demonstrate hypermethylation across various human cancers, including GBM[54]. Analysis of the TCGA GBM dataset revealed a negative correlation between the mRNA levels of *CGAS* and *STING* and their respective methylation statuses (Fig. 7g, h). DNA methylation processes are predominantly governed by DNA methyltransferases (DNMTs), whereas demethylation is facilitated by ten-eleven translocation (TET) dioxygenases[55]. Notably, within the TET family, TET2 and TET3 exhibited a positive correlation with the expression of cGAS and STING in GBM samples from both TCGA and CGGA datasets. However, no inverse relationship was found between cGAS or STING expression and DNMT levels (Supplementary Fig. 10a, b). To explore the regulation of cGAS and STING expression by TET dioxygenases, we conducted experiments involving the overexpression of TET1, TET2, and TET3 in HEK293T cells (Supplementary Fig. 10c). Remarkably, the overexpression of TET3 led to a significant enhancement of cGAS and STING expression compared to TET1 and TET2 (Fig. 7i). Conversely, the KD of TET3, rather than TET1 or TET2, resulted in a substantial reduction in cGAS and STING expression (Fig. 7j).

To determine if TET3 undergoes CMA-mediated proteolysis, we examined its sequence for the presence of putative KFERQ-like motifs. We compared the motifs and found that TET3 possesses such motifs (Supplementary Table 1). Given that CMA substrates are recruited to the lysosome via HSC70, we investigated the potential interaction between HSC70 and TET3. Wild-type TET3 was found to interact with both HSC70 and LAMP2A; however, the mutation in the KFERQ-like motifs of TET3 (Supplementary Table 1) disrupted these interactions (Fig. 7k), leading to enhanced stability of TET3 protein upon treatment with CHX (Fig. 7l, m). Furthermore, KD of LAMP2A or HSC70 in GSCs resulted in a diminished association of TET3 with lysosomes and an upregulation of total TET3 protein level (Fig. 7n, o). Importantly, neither the depletion of LAMP2A nor HSC70 caused notable alterations in *TET3* mRNA levels (Supplementary Fig. 10d, e). Conversely, the overexpression of both LAMP2A-WT and the 3D mutant resulted in decreased TET3 levels in HEK293T cells, whereas the LAMP2A-3A and 4 A mutants did not have this effect (Supplementary Fig. 10f). Furthermore, the co-localization of TET3 with lysosomes that express LAMP2A during CMA-inducing conditions, such as nutrient deprivation, was disrupted when the KFERQ motifs were altered (Supplementary Fig. 10g, h). Treatment with lysosomal protease inhibitor LN increased TET3 protein level after CHX treatment, indicating that TET3 degradation is mediated by CMA (Fig. 7p). In contrast, neither the proteasome inhibitor (MG132) nor the macroautophagy inhibitor (3-MA) had this effect (Fig. 7p). When purified TET3 protein was incubated with lysosomes, either untreated or pre-treated with PI, immunoblot analysis of the recovered lysosomes indicated that TET3 was taken up and degraded by them (Supplementary Fig. 10i, j).

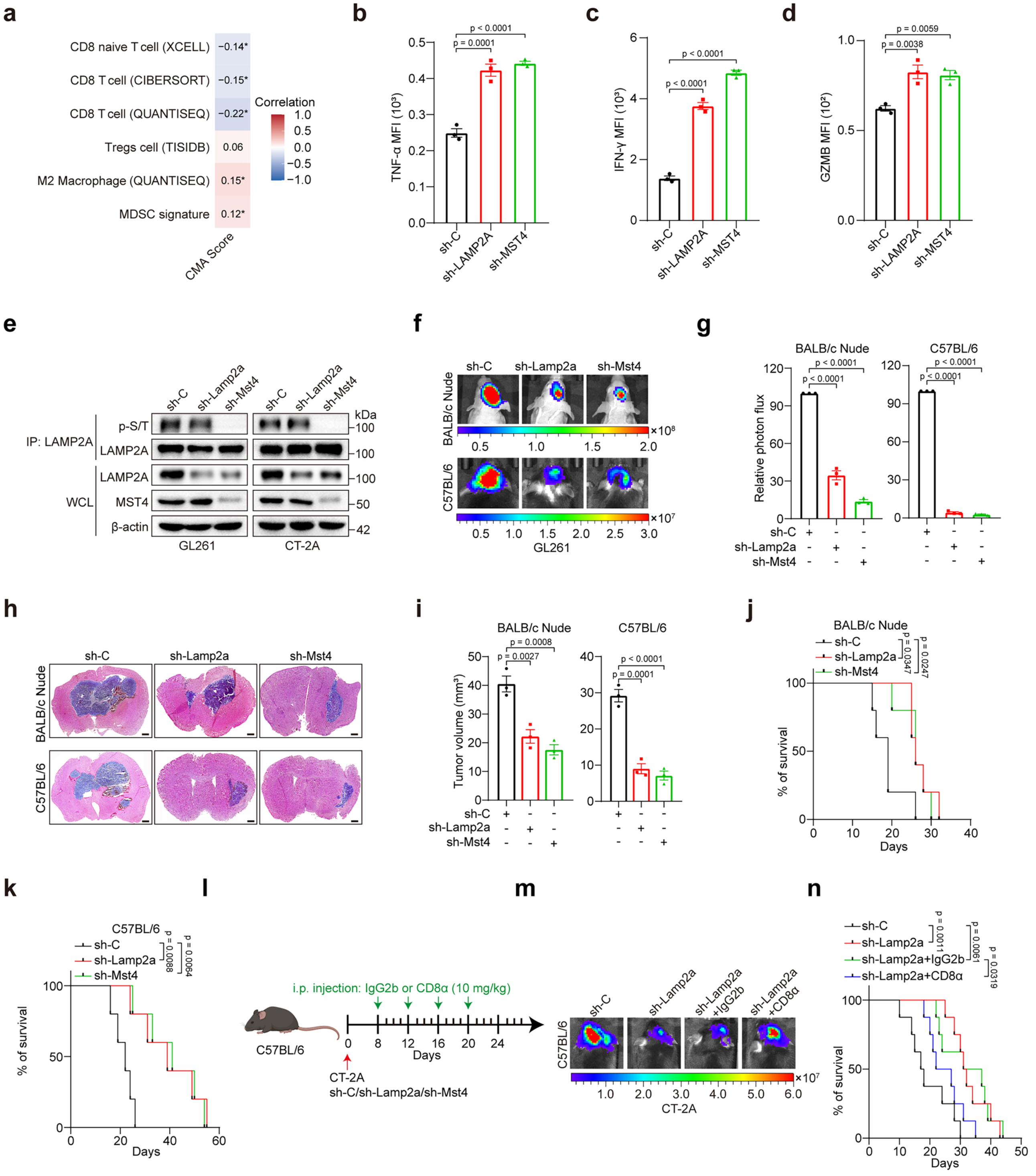

Collectively, these results support the conclusion that TET3 is a substrate for CMA.

Phosphorylation of LAMP2A by MST4 inhibits cGAS-STING signaling by repressing TET3 expression

To investigate whether CMA inhibits the cGAS-STING pathway via TET3 suppression, we established individual KD GSC cell lines targeting TET3 (Supplementary Fig. 11a). Our findings revealed that KD of MST4 or LAMP2A enhanced, while KD of TET3 diminished, the level of herring testis DNA (HT-DNA) or the IR-induced activation of cGAS-STING signaling, as indicated by the phosphorylation of TBK1 and STING (Supplementary Fig. 11b, c). Furthermore, TET3 KD mitigated the impact of MST4 or LAMP2A KD on IR-triggered activation of cGAS-STING pathway (Fig. 8a–d), suggesting that TET3 is essential for CMA's suppression of cGAS-STING signaling. In a parallel experiment, pharmacological inhibition of CMA using Polyphyllin D (PPD), a potential inhibitor of CMA that disrupts the binding between HSC70 and LAMP2A and inhibits LAMP2A homo-multimerization[47], was found to enhance cGAS-STING signaling in GSC M83 and 456 cell lines. Our results showed that MST4-mediated phosphorylation facilitates LAMP2A multimerization, which is essential for CMA activation; however, PPD selectively interferes with the downstream multimerization process without affecting LAMP2A phosphorylation (Supplementary Fig. 11d, e). Furthermore, PPD disrupted the HSC70-LAMP2A complex,

Fig. 6 | CMA inhibition attenuates GBM tumorigenicity by augmenting anti-tumor immunity. a Spearman correlation heatmap between CMA activity scores and immune infiltration levels in TCGA-GBM dataset. Color gradient represents correlation coefficients, with numerical values and statistical significance (*p*-values) annotated. GSC M83 cells with indicated modification were co-cultured for 24 hours with or without CD8$^+$ T cells isolated from GBM patients' peripheral blood. Flow cytometry quantified T cell-derived: TNF-α (**b**), IFN-γ (**c**), and GZMB (**d**) production. $n = 3$ independent experiments. MFI, mean fluorescence intensity. **e** IP-IB analyses for indicated proteins in GL261 and CT-2A cells expressing sh-C, sh-Mst4 or sh-Lamp2a. **f** Representative luciferase-based bioluminescence images of athymic (BALB/c Nude) mice (top) or C57BL/6 mice (bottom) intracranially transplanted with GL261 cells expressing sh-C, sh-Lamp2a or sh-Mst4. Colored scale bars represent photons/s/cm^2/steradian. **g** Relative photon flux of athymic (BALB/c Nude) mice (left) or C57BL/6 mice (right) intracranially transplanted with GL261 cells with indicated modifications. $n = 3$ mice per group. **h, i** Representative H&E images of mouse brain sections (**h**) and quantification of tumor volume (**i**) from athymic (BALB/c Nude) mice or C57BL/6 mice intracranially implanted with GL261 cells expressing sh-C, sh-Lamp2a or sh-Mst4. $n = 3$ mice per group. Scale bar, 1.0 mm. **j, k** Kaplan-Meier survival curves of athymic (BALB/c Nude) mice (**j**) or C57BL/6 mice (**k**) intracranially transplanted with GL261 cells expressing sh-C, sh-Lamp2a or sh-Mst4. $n = 5$ mice per group. **l** Scheme representing the experimental procedure, created with BioRender.com. **m** Representative luciferase-based bioluminescence images of C57BL/6 mice intracranially transplanted with CT-2A cells with indicated modifications and treatments. Colored scale bars represent photons/s/cm^2/steradian. **n** Kaplan-Meier survival curves of C57BL/6 mice intracranially transplanted with CT-2A cells with indicated modifications and treatments. $n = 8$ mice per group. All the experiments showed consistent results in at least three independent biological replicates. Statistical significance was assessed using one-way ANOVA with Dunnett's multiple comparisons test (**b–d, g, i**) or log-rank test (**j, k, n**). Source data are provided as a Source Data file.

resulting in the cytosolic accumulation of CMA substrates, including TSC1/2, TET3, and MEF2D, accompanied by a decrease in lysosomal delivery and CMA flux, as evidenced by photo-convertible reporter assays (Supplementary Fig. 11e–g). Thus, PPD effectively decouples MST4-mediated LAMP2A phosphorylation from functional CMA activation. Additionally, TET3 KD was found to inhibit the PPD-induced activation of cGAS-STING signaling (Fig. 8e, f).

To elucidate the role of MST4-mediated phosphorylation of LAMP2A in modulating cGAS-STING signaling, we assessed the alterations in cGAS-STING pathway activity following IR stimulation in LAMP2A-KD GSC M83 cells reconstituted with either LAMP2A-WT or LAMP2A-3D, subsequently subjected to MST4 KD. In GSC M83 cells expressing LAMP2A-WT instead of LAMP2A-3D, MST4 KD significantly enhanced the activation of the cGAS-STING signaling pathway in response to IR (Fig. 8g, h). Additionally, the KD of endogenous LAMP2A in GSC 23 cells resulted in an enhancement of IR-induced STING/TBK1 activation and an upregulation of IFNB1 expression. In contrast, the overexpression of exogenous MST4 inhibited the activation of the cGAS-STING pathway in GSC 23 cells, and these effects were attenuated by the KD of endogenous LAMP2A (Fig. 8i, j).

Subsequently, we investigated whether the KD of TET3 or cGAS could counteract the influence of LAMP2A KD on in vivo tumor proliferation. In an immunocompetent murine model of intracranial GBM, we demonstrated that Lamp2a KD significantly suppressed GL261 cell proliferation and tumorigenesis in vivo, while extending mouse survival from 22 to 38 days (Fig. 8k, l and Supplementary Fig. 11h-j). Notably, in vitro experiments revealed that Cgas (but not Tet3) KD had no impact on GL261 proliferation regardless of Lamp2a status (Supplementary Fig. 11h–j). However, in vivo Tet3 or Cgas KD promoted tumor growth, reduced intratumoral CD8$^+$ T cell infiltration, and shortened survival (Fig. 8k–m). Collectively, these findings indicated that CMA modulates tumor progression, at least in part, through TET3-cGAS-STING signaling pathway.

CMA inhibition enhances radiotherapy and immune checkpoint therapy in a murine GBM model

Based on our findings, we proposed a model wherein CMA functions as an inhibitor of the anti-tumor immune response by restricting the activation of the cGAS-STING pathway. Supporting this hypothesis, both GSC M83 and GSC 456, as well as GL261 cells with LAMP2A KD, exhibited elevated levels of *IFNB1*, *CCL5*, *CXCL10*, and the immune checkpoint ligand *PD-L1* (CD274), while no significant change was observed in *PD-L2* expression (Supplementary Fig. 12a). Furthermore, knocking down endogenous Mst4 or Lamp2a in murine syngeneic GBM cell lines GL261 and CT-2A resulted in a significant increase in the levels of CMA substrates TET3 and TSC1/2 (Supplementary Fig. 12b). Upon intracranial implantation of these genetically altered cells into immunocompetent C57BL/6 mice, the absence of Mst4 or Lamp2a led to a marked elevation of TET3 and TSC1/2 expression in the tumors, as confirmed by immunofluorescence analysis of murine tissues (Supplementary Fig. 12c). We then explored whether CMA inhibition would enhance the efficacy of IR or immune checkpoint therapy (ICT) in GBM. Mice with intracranial GL261 and CT-2A xenografts, in the presence or absence of endogenous Mst4 or Lamp2a, were received either IR therapy, or anti-PD-1 monoclonal antibody (mAb), or their combination and were monitored tumor growth and mouse survivals (Fig. 9a and Supplementary Fig. 12d). Notably, neither IR therapy nor anti-PD-1 mAb monotherapy effectively impeded tumor proliferation or enhanced mice survivals. Conversely, the simultaneous administration of IR and anti-PD-1 mAb resulted in a moderate yet statistically significant ($p < 0.05$) survival advantage in immunocompetent mice bearing intracranial GL261 and CT-2A GBM cells (Fig. 9b, c and Supplementary Fig. 12e, f). Genetic ablation of Mst4 or Lamp2a to inhibit CMA significantly potentiated the anti-tumor efficacy and survival benefits of either IR alone, anti-PD-1 monoclonal antibody (mAb) monotherapy, or their combination in GL261 and CT-2A GBM models (Fig. 9b–e and Supplementary Fig. 12e–h).

Given that PPD effectively inhibits the multimerization of LAMP2A, which is a consequence of LAMP2A phosphorylation, we investigated the effects of the CMA inhibitor PPD on IR therapy and anti-PD-1 mAb therapy in the GL261 and CT-2A C57BL/6 intracranial GBM model. The treatment of PPD, IR, and anti-PD-1 mAb were given as monotherapies, in combination, or as a triplet regimen (Fig. 9f and Supplementary Fig. 12i). The results showed that all combination therapy strategies, rather than monotherapy, significantly attenuated tumor growth compared with the control group, with the greatest survival advantage observed in the trimodal treatment group (Fig. 9g, h and Supplementary Fig. 12j, k). As anticipated, the significant tumor shrinkage linked to combination treatment was associated with a higher presence of CD8$^+$ cytotoxic T lymphocytes in the tumor microenvironment (Fig. 9i). Additionally, xenografts treated with the CMA inhibitor PPD exhibited increased expression of the CMA substrates TET3 and TSC1/2, indicating PPD's ability to penetrate the blood-brain barrier (BBB) and reduce GSC tumorigenicity by inhibiting the CMA-mediated degradation of TET3 and TSC1/2 in the xenografts (Supplementary Fig. 12l, m). In summary, our findings indicated that the combination of CMA inhibition with anti-PD-1 or IR presents a promising avenue for cancer therapeutic.

Correlations between MST4, p-LAMP2A, TET3 and TSC1/2 expression and associations with GBM patient survival

To explore the prognostic significance of our results, we conducted immunohistochemical (IHC) staining for LAMP2A pT136, MST4, TET3, and TSC1/2 in tumor sections from GBM patients (Fig. 10a and Supplementary Dataset). Our analysis of human glioma samples demonstrated a positive association between the staining levels of MST4 and LAMP2A pT136. Furthermore, we observed a negative correlation between LAMP2A pT136 level and both TET3 and TSC1/2 (Fig. 10b). The

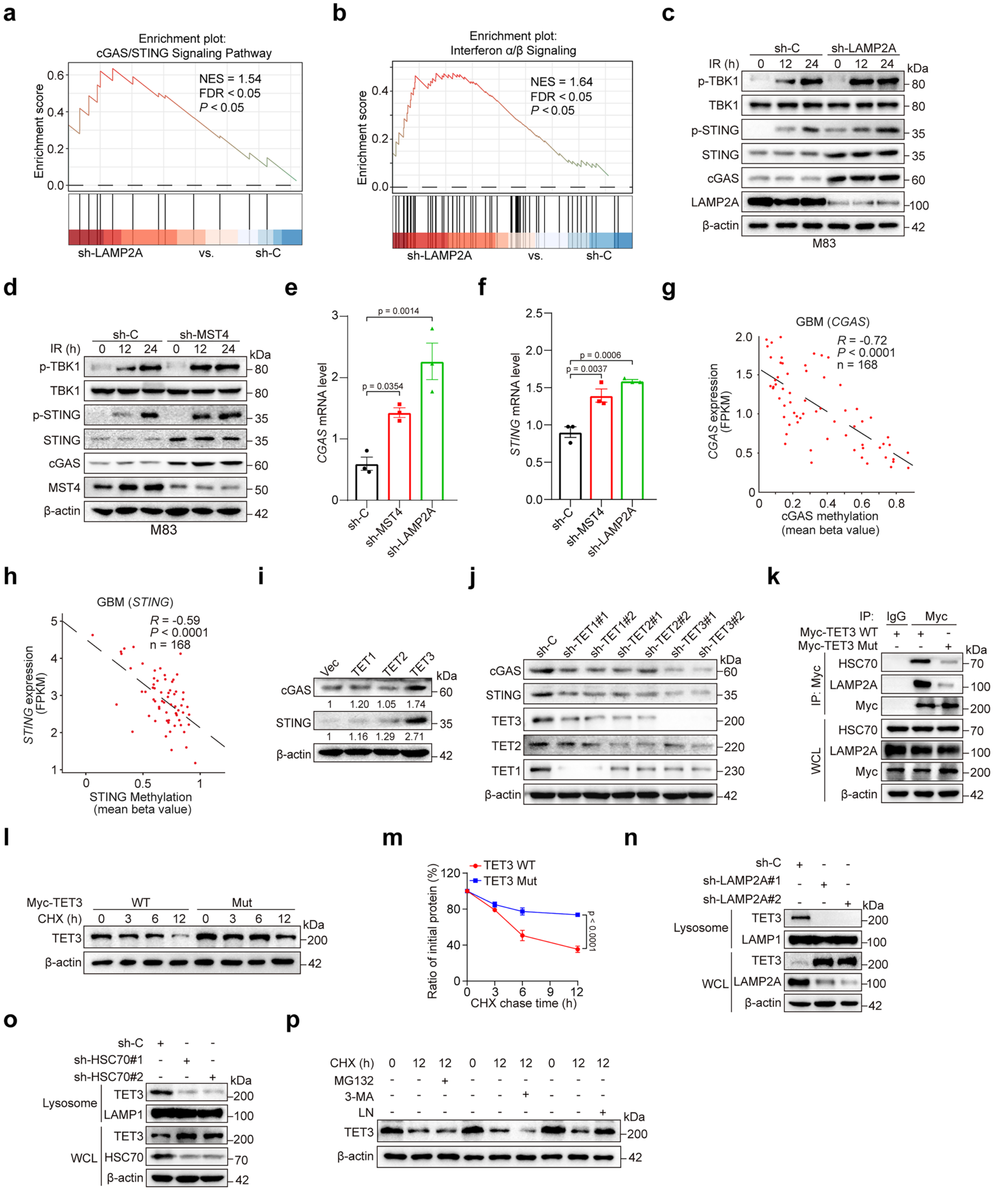

clinical relevance of these observations was highlighted by the finding that patient survival demonstrates an inverse relationship with the expression levels of MST4 and phosphorylated LAMP2A, while showing a positive association with the expression levels of TET3 and TSC1/2 as determined by IHC staining (Fig. 10c).

Discussion

This study provided evidence that the MST4-LAMP2A signaling pathway in GSCs regulates CMA activity, cell proliferation, and tumorigenicity. Mechanistically, our results elucidated three critical processes: Firstly, MST4 promotes the oligomerization and stabilization of LAMP2A via phosphorylation at the T40, S97 and T136 residues, thereby augmenting CMA activity within GSCs. Secondly, we identified TSC1/2 as CMA substrates; their degradation enhances mTORC1 signaling activity, which is crucial for maintaining the stemness of GSCs. Furthermore, CMA inhibits the cGAS-STING pathway and dampens anti-tumor immunity by targeting TET3. The knockdown of MST4 or LAMP2A, or the pharmacological inhibition of CMA using PPD,

Fig. 7 | CMA regulates the cGAS/STING signaling pathway through targeting TET3. GSEA enrichment plots for the cGAS/STING signaling pathway (**a**) and the interferon α/β signaling cascade (**b**) in GSCs lacking LAMP2A. **c, d** Impact of IR (6 Gy) on the activation of STING/TBK1 in GSC M83 cells, both with and without LAMP2A KD (**c**) or MST4 KD (**d**). **e, f** Quantitative real-time PCR (qRT-PCR) analysis of mRNA levels of *CGAS* (**e**) and *STING* (**f**) in GSC M83 cells transduced with sh-C, sh-MST4 or sh-LAMP2A. $n = 3$ independent experiments. Analysis of the relationship between mRNA levels and methylation status of *CGAS* (**g**) and *STING* (**h**) in GBM samples derived from TCGA datasets. **i** IB analyses for cGAS and STING in HEK293T cells transfected with Vec, TET1, TET2 or TET3. Band intensities of indicated proteins were quantified using Image J, normalized to β-actin. **j** IB analyses for indicated proteins in HEK293T cells with indicated modifications. **k** IP-IB for indicated proteins in HEK293T cells overexpressing Myc-TET3 wild-type (WT) or mutant variant (Mut). **l** IB analysis for TET3 in HEK293T cells overexpressing Myc-TET3-WT or -Mut, following treatment with CHX (100 μg/mL) for indicated time. **m** Quantification of TET3 protein level in HEK293T cells with indicated modifications and treatments. $n = 3$ independent experiments. IB analyses for indicated proteins in WCL and lysosomal fractions of GSC M83 cells with or without LAMP2A KD (**n**) or HSC70 KD (**o**). **p** IB analysis for TET3 in GSC M83 cells, either untreated or subjected to 10 μM MG132, 5 mM 3-MA or LN (10 μM leupeptin and 20 mM NH_4Cl) for an additional 12 hours post-CHX (100 μg/mL) treatment for 12 h. Data are presented as the means ± S.E.M. All the experiments showed consistent results in at least three independent biological replicates. Statistical significance was assessed using two-sided Kolmogorov-Smirnov test (**a, b**), one-way ANOVA with Dunnett's multiple comparisons test (**e, f**), two-sided Pearson correlation test (**g, h**) or two-way ANOVA with Bonferroni's multiple comparisons test (**m**). Source data are provided as a Source Data file.

significantly inhibits tumor growth in an orthotopic GBM mouse model (Fig. 10d). This inhibitory effect is further enhanced when combined with IR and anti-PD-1 therapy.

CMA, as a component of the cellular stress response, plays a crucial role in sustaining cellular homeostasis. Baseline CMA activity facilitates the lysosomal degradation of fully functional proteins, effectively terminating their activity and thereby modulating various cellular processes, including metabolic pathways, cellular differentiation, and circadian rhythms[10,56,57]. LAMP2A is the only known lysosomal receptor for CMA. Precise regulation of LAMP2A level within the lysosome is crucial for modulating CMA activity. Nonetheless, the specific mechanisms governing the dynamic alterations of LAMP2A at the lysosome remain inadequately understood. Our study elucidated that MST4, a constituent of the GCKIII subfamily, functions as a regulator that enhances CMA activity by sustaining a baseline expression of LAMP2A within lysosomal compartments. We observed that serum stimulation interfered with the interaction between MST4 and LAMP2A, whereas deprivation of growth factors (EGF/FGF) did not produce the same effect. Evidence suggested that serum inhibits the autophosphorylation and kinase activity of MST4, a process mediated by the striatin (STRN)-interacting phosphatase and kinase (STRIPAK) complex[58–60]. In this context, STRIPAK might act as a mediator for MST4-mediated CMA response to the serum stimulation. MST4, which is localized within the Golgi apparatus, plays a role in various cellular signaling pathways and pathologies[25].

The homomultimerization of LAMP2A has been demonstrated to play a crucial role in the subsequent translocation of its substrates into the lysosome lumen[61,62]. Both the membrane-distal subdomains (N-domain) and the membrane-proximal subdomain (C-domain) within the lumenal region of LAMP2A are integral to its homomultimerization and its functional properties. Our observations indicated that the phosphorylation sites on LAMP2A (T40, S97, and T136) targeted by MST4 are situated within the N-domain. It is plausible that MST4-mediated phosphorylation of LAMP2A may influence its local conformation, thereby facilitating the homo-oligomeric association of LAMP2A and, ultimately, enhancing CMA activity. Moreover, MST4 appears to preserve the basal level of LAMP2A within lysosomes by inhibiting the binding and subsequent cleavage of LAMP2A by Cathepsin A, which results in diminished degradation and an overall elevation of LAMP2A abundance in lysosomes. The expression of MST4 (*STK26*) in GSCs has been previously shown to be negatively regulated by DNA methylation within its promoter region, a suppression that can be attenuated following IR treatment[27]. Either constitutively expressed or induced MST4 phosphorylates LAMP2A, thereby stabilizing it and promoting its multimerization. This process subsequently activates CMA, enhances self-renewal capabilities, and increases the tumorigenic potential of GSCs, while also bolstering the resistance of GBM to ICT.

Although CMA has been associated with the self-renewal and differentiation of normal stem cells[63], investigations into CMA within cancer stem cells remain limited, Emerging evidence indicates that CMA plays a role in GBM, where LAMP2 shows upregulated expression in both human GBM tissues and GSCs. Functional studies reveal that the depletion of LAMP2A not only diminishes the activity of patient-derived GSCs but also disrupts multiple biological pathways and processes[17,64]. However, the underlying molecular mechanisms driving GBM malignancy have yet to be fully elucidated. In this study, we used multiple approaches to measure CMA activity and confirmed that elevated CMA is crucial for preserving the stem cell characteristics of GSCs. Proteomic and transcriptomic analyses of GSCs deficient in LAMP2A indicated diminished mTORC1 activity across both platforms. It has been established that mTORC1 plays a significant role in sustaining cancer stem cells[65–67]. Our findings revealed that TSC1 and TSC2, which act as the upstream negative modulators of mTORC1, contain CMA-targeting motifs (KFERQ-like motifs). Enhanced levels of TSC1 and TSC2 were observed in GSCs subjected to LAMP2A or MST4 KD. Mutations within the KFERQ-like motifs of TSC1 and TSC2 disrupted their interaction with HSC70 and LAMP2A, leading to suppressed proliferation, self-renewal, and tumorigenic potential of GSCs. Thus, we proposed that CMA is instrumental in sustaining the malignancy of GSCs by mediating the lysosomal degradation of TSC1/2 and subsequently activating the mTORC1 pathway. Notably, TSC2 is also subjected to degradation via the ubiquitin-proteasome pathway, a process regulated by TSC2 phosphorylation by AKT, which is activated by growth-promoting signals such as insulin[68]. It is plausible that the relative impact of these two proteolytic mechanisms, the proteasome and CMA, on the regulation of TSC2 level is contingent upon the specific cell type and stimuli, or that both pathways function in a coordinated sequential manner.

Activation of cGAS-STING signaling pathway can promote T cell infiltration and enhance anti-tumor immune response[69]. However, in GBM or other tumors, the cGAS-STING pathway is often silenced due to the methylation of the promoters of *CGAS* or *STING*, contributing to the "cold response" of these tumors to immunotherapy. The molecular mechanisms underlying the downregulation of cGAS or STING are not well understood. In this study, we elucidated the pivotal function of CMA in the methylation of *CGAS/STING* by targeting the DNA demethylase TET3, thereby inhibiting cGAS/STING-mediated DNA sensing pathways and facilitating tumor immune evasion. Our findings indicated that the efficacy of anti-PD-1 therapy is significantly enhanced in cold, nonresponsive tumors when combined with genetic or pharmacological inhibition of CMA in murine models. Some of the most widely used anti-tumor therapies in clinical practice, such as radiotherapy, PARP inhibitors (PARPi), and DNA-damaging chemotherapeutics, have been documented to activate cGAS-STING signaling, thereby augmenting tumor immunogenicity[70–74]. Given that the baseline activity of cGAS-STING signaling in tumors is partially suppressed due to CMA-mediated methylation of *CGAS/STING*, inhibiting CMA emerges as a

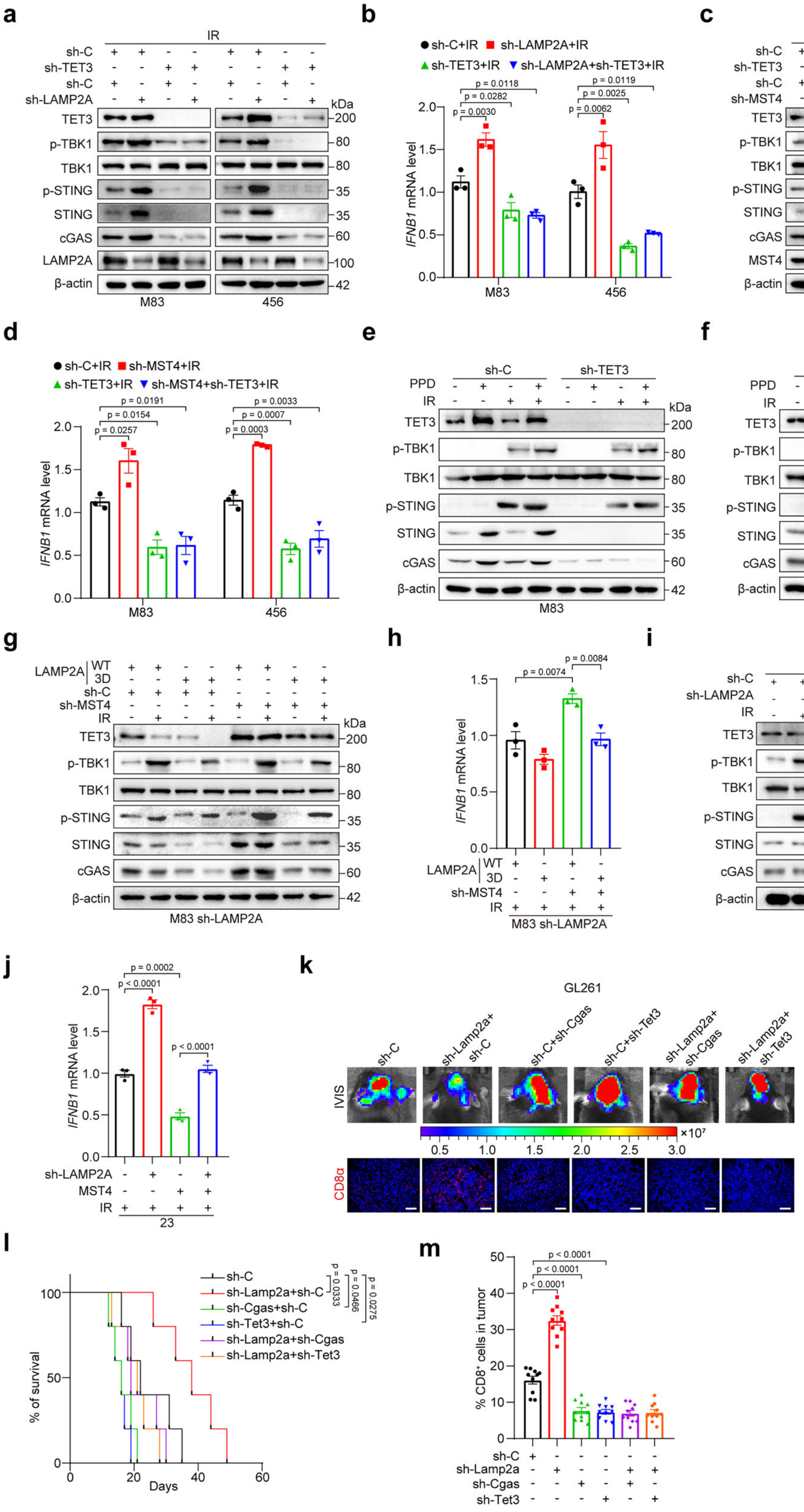

compelling therapeutic strategy to potentially enhance the effectiveness of these DNA-damaging modalities, thereby improving the immunogenic landscape of the tumor microenvironment for cancer patients. In GL261/CT-2A xenograft tumor models, the treatment of PPD, a selective CMA inhibitor that obstructs HSC70-LAMP2A interactions and LAMP2A homo-multimerization[75], in conjunction with radiotherapy, effectively activated the cGAS-STING pathway and augmented the response to anti-PD-1 therapy, as evidenced by significant infiltration of CD8$^+$ T cells into the tumor microenvironment. While our study primarily focuses on CD8$^+$ T cells, we acknowledge that other immune cell populations, including Tregs, MDSCs, and TAMs, may also participate in CMA-mediated immune modulation within the tumor microenvironment. Future studies incorporating human glioma xenograft models would provide

Fig. 8 | MST4 phosphorylation of LAMP2A suppresses cGAS-STING signaling by downregulating TET3 expression. a, c IB analyses for indicated proteins in GSC M83 and 456 cells subjected to the indicated modifications after 6 Gy IR treatment. **b, d** qRT-PCR analysis of *IFNB1* mRNA level in GSC M83 and 456 cells with indicated modifications after 6 Gy IR exposure. *n* = 3 independent experiments. IB analyses for indicated proteins in GSC M83 (**e**) and 456 (**f**) cells with or without TET3 KD, Polyphyllin D (PPD, 3.2 μM) treatment or 6 Gy IR exposure. **g, i** IB analyses for indicated proteins in GSC M83 (**g**) and 23 (**i**) cells with indicated modifications, with or without 6 Gy IR exposure. qRT-PCR analysis of *IFNB1* mRNA level in GSC M83 (**h**) and 23 (**j**) cells with indicated modifications following 6 Gy IR exposure. *n* = 3 independent experiments. **k** The upper panel shows representative luciferase-based bioluminescence images of C57BL/6 mice with intracranially implanted GL261 cells under specified conditions. The colored scale bars indicate photons/s/cm²/steradian. The lower panel displays representative IF staining images for CD8⁺ cells in tumor tissues, with a scale bar of 100 μm. **l** Kaplan-Meier survival curves of C57BL/6 mice intracranially transplanted with GL261 cells with indicated modifications. *n* = 5 mice per group. **m** Quantitative analysis of CD8⁺ cells in tumor tissues from C57BL/6 mice with GL261 cells under specified conditions, based on 10 randomly selected microscopic fields. Data are presented as the means ± S.E.M. All the experiments showed consistent results in at least three independent biological replicates. Statistical significance was assessed using one-way ANOVA with Dunnett's multiple comparisons test (**b, d, m**), one-way ANOVA with Tukey's multiple comparisons test (**h, j**) and log-rank test (**l**). Source data are provided as a Source Data file.

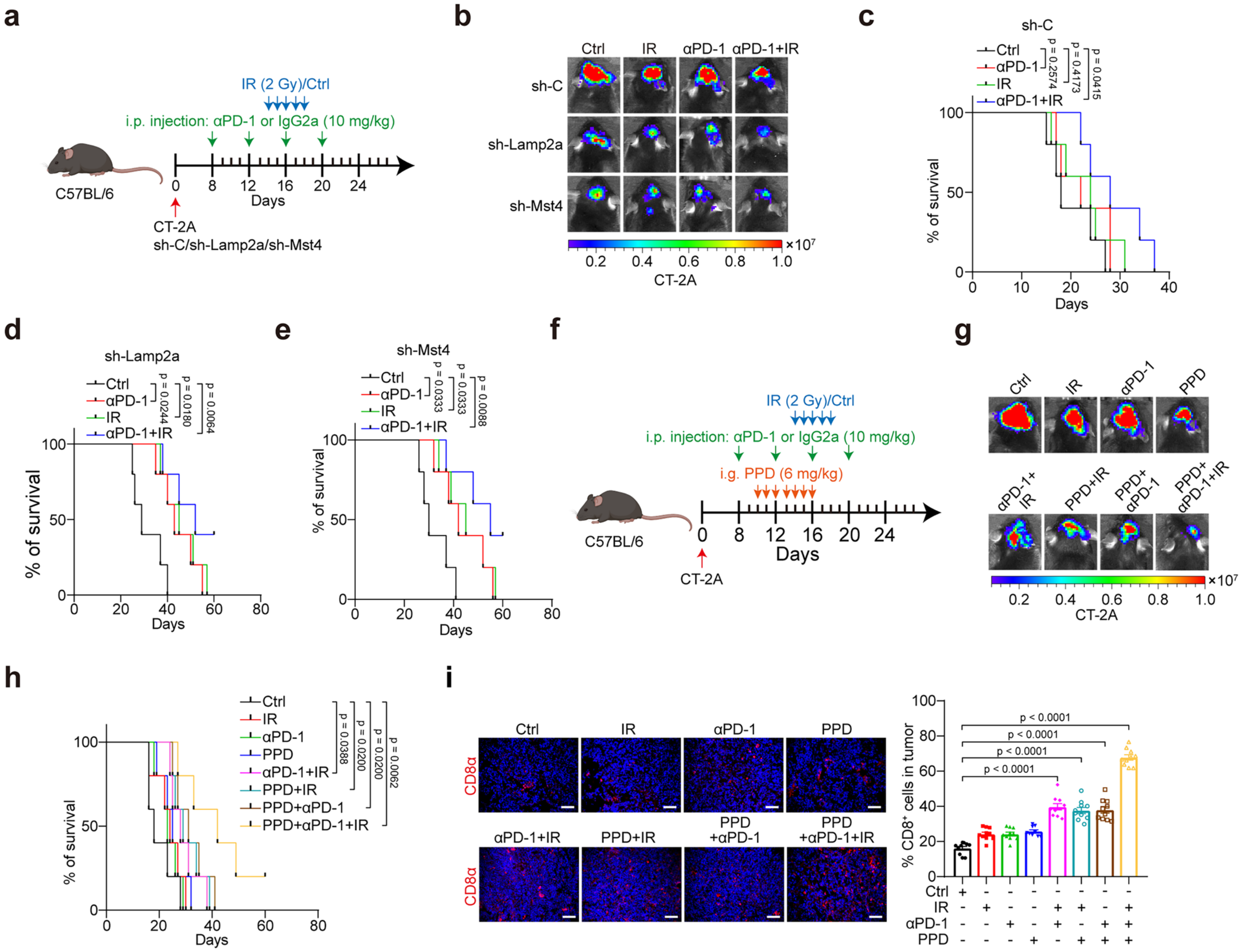

Fig. 9 | Inhibition of CMA potentiates the therapeutic efficacy of IR and ICT. a, f Scheme representing the experimental procedure, created with BioRender.com. **b** Representative luciferase-based bioluminescence images of C57BL/6 mice with intracranially transplanted CT-2A cells with indicated modifications and treatments. Colored scale bars represent photons/s/cm²/steradian. **c-e** Kaplan-Meier survival curves of C57BL/6 mice with intracranially transplanted with CT-2A cells with modifications and treatments. *n* = 5 mice per group. **g** Representative luciferase-based bioluminescence images of C57BL/6 mice with intracranially transplanted CT-2A cells with indicated treatments. Colored scale bars represent photons/s/cm²/steradian. **h** Kaplan-Meier survival curves of C57BL/6 mice with intracranially transplanted with CT-2A cells with indicated treatments. *n* = 5 mice per group. **i** Representative IF staining images for CD8⁺ cell staining in tumor tissues (left) and the corresponding quantification of CD8⁺ cells in C57/BL6 mice with intracranial GL261 cells transplants under various treatments (right). Data are presented as the mean ± S.E.M. *n* = 10 randomly selected microscopic fields. Scale bar, 100 μm. All the experiments showed consistent results in at least three independent biological replicates. Statistical significance was assessed using log-rank test (**c-e, h**) or one-way ANOVA with Dunnett's multiple comparisons test (**i**). ns, not significant. Source data are provided as a Source Data file.

valuable complementary data to further elucidate the comprehensive role of CMA in shaping the immunosuppressive tumor niche. These cell types represent important avenues for future investigation into the comprehensive immunoregulatory functions of CMA. These findings support CMA as a viable immunotherapeutic target and highlighted an important clinical opportunity to combine CMA inhibition, IR, and anti-PD-1 therapy for treating "cold tumors" that exhibit resistance to PD-1 therapy. Although PPD is known as a CMA-targeting inhibitor[75], its specificity may be limited since it could affect other cellular stress pathways[76]. This reflects a broader challenge in the field due to the lack of highly selective CMA inhibitors[10]. The recent identification of CIM7[77], which selectively inhibits CMA

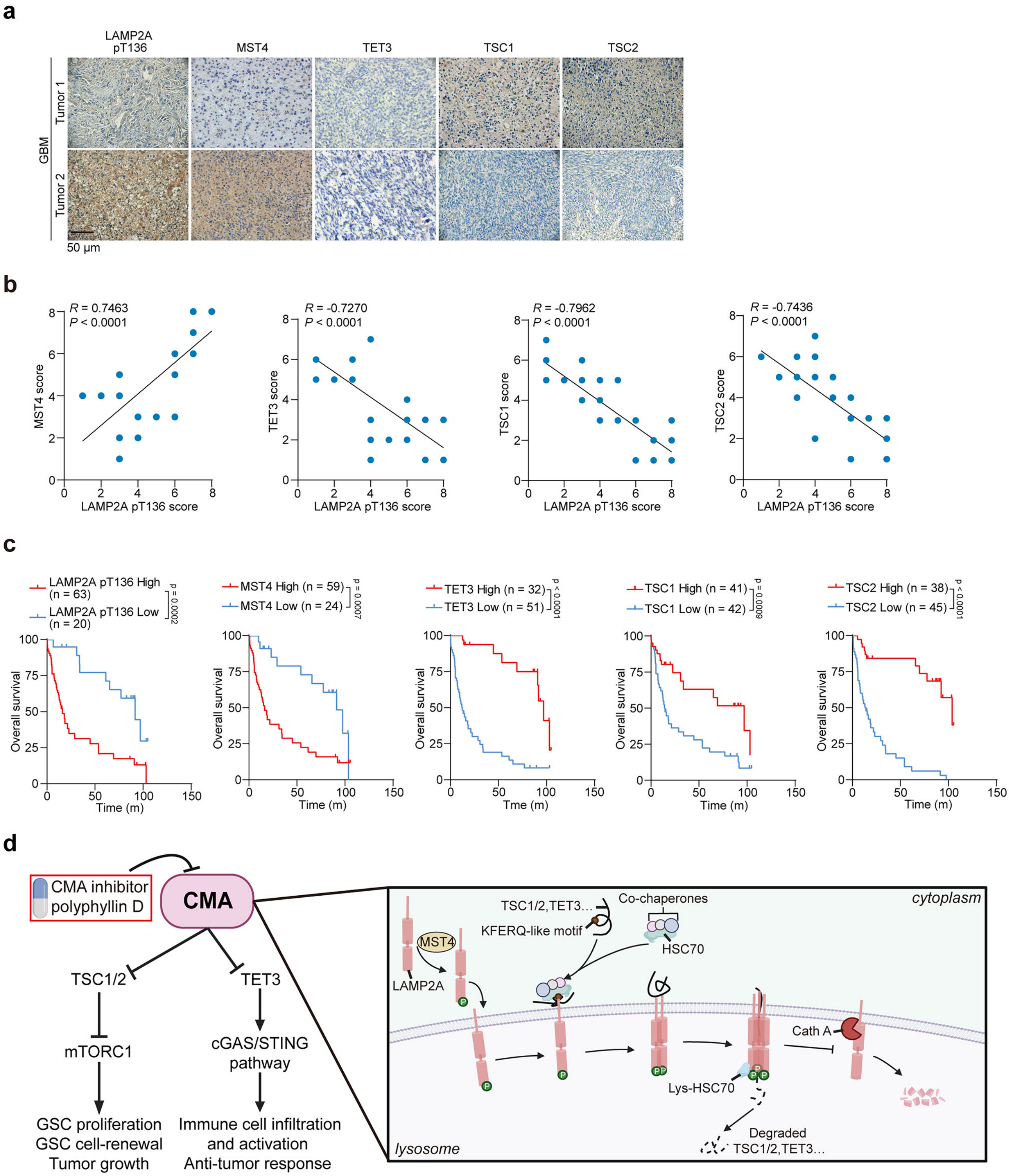

Fig. 10 | The prognostic significance of the correlative expression levels of MST4, p-LAMP2A, TSC1/2, and TET3 in clinical glioma. **a** Representative immunohistochemical (IHC) staining images of phosphorylated LAMP2A (LAMP2A pT136), MST4, TET3, TSC1 and TSC2 in clinical glioma specimens. Scale bar, 50 μm. **b** Scoring of IHC staining of human glioma samples using the specified antibodies, followed by correlation analysis utilizing a two-tailed Pearson correlation test. $n = 83$ glioma samples. Note that some sample scores may overlap. **c** Kaplan-Meier survival analyses for glioma patients categorized by high or low expression levels of LAMP2A pT136, MST4, TET3, TSC1 and TSC2. $n = 83$ glioma samples. IHC score ≥ 4 was considered as high expression samples, IHC score ≤ 3 was considered as low expression samples. Statistical significance was assessed using log-rank test. **d** Schematic representation of the MST4-LAMP2A signaling axis in modulating mTORC1 and cGAS/STING pathways, as well as its impact on GBM tumorigenesis, created with BioRender.com. Source data are provided as a Source Data file.

without impacting macroautophagy, represents a significant advancement, positioning CIM7 as a promising candidate for future studies on CMA-targeted therapies for GBM, potentially addressing the limitations of PPD.

The clearance of apoptotic cells (ACs) by efferocytes, including macrophages and dendritic cells, is termed "efferocytosis". This process fosters an immunosuppressive tumor microenvironment (TME) and enables immune evasion by cancer cells[78]. Notably, autophagy has been evidenced to be crucial for the proficient clearance of ACs by activated inflammatory cells such as neutrophils and macrophages[79,80]. Interestingly, autophagy-related components have been identified on phagosomes harboring apoptotic cells and are indispensable for both AC degradation and subsequent immune modulation[81]. Specifically, LC3-associated phagocytosis (LAP), where the autophagy marker LC3 attaches to phagosomes, affects the transformation of TAMs into immunosuppressive types. LAP also inhibits STING-mediated type I interferon responses in TAMs, which are critical for the anti-tumor responses observed upon LAP disruption[82,83]. In this study, we demonstrate that CMA facilitates the hypermethylation of *CGAS/STING* by promoting the lysosomal degradation of the DNA demethylase TET3, thereby inhibiting cGAS/STING-mediated DNA sensing pathways and contributing to the establishment of the immunosuppressive microenvironment typical of GBM. Given the crucial role of autophagy in the efferocytosis process that clears apoptotic cells resulting from DNA-damaging treatments like radiotherapy, it is worthwhile to further explore whether CMA influences both the cGAS/STING pathway and the anti-tumoral immune response via efferocytosis in myeloid cells. The interplay between CMA and efferocytosis opens up potential therapeutic avenues for combating the immunosuppressive TME in GBM.

In summary, our study elucidated the MST4-LAMP2A regulatory axis as a pivotal determinant of CMA activity, while also uncovering a key role of CMA as an inherent modulator of GSC malignancy and anti-tumor immunity, thereby proposing a promising therapeutic approach aimed at targeting CMA for cancer treatment.

Methods

Reagents and antibodies

The chemicals and their sources are as follows: leupeptin (HY-18234; 10 μM), NH_4Cl (HY-Y1269; 20 mM), Pepstatin (HY-P0018, 10 μM), 3-MA (3-methyladenine) (HY-19312; 5 mM), MG132 (HY-13259; 10 μM), CHX (cycloheximide) (HY-12320; 100 μg/mL) and SB203580 (HY-10256; 10 μM) were purchased from MCE. HT-DNA (Herring testis DNA) (D6898; 100 μg/mL), general protease inhibitors (P8340; 1:100), phosphatase inhibitors (P0044; 1:100) and AEBSF (SBR00015; 100 μM) were purchased from Sigma-Aldrich. D-luciferin potassium salt (115144-35-9; 150 mg/kg in vivo) was purchased from GoldBio. Polybrene (28728-55-4; 6 mg/mL) was purchased from Santa Cruz Biotechnology. Puromycin (S250J0; 1 mg/mL) was purchased from Basalmedia. PPD (polyphyllin D) (50773-41-6; 6 mg/kg in vivo) was purchased from Yuanye.

The antibodies for immunoblot (IB) were provided as follows: anti-LAMP2A (ab125068; 1:1,000) and veriBlot for IP Detection Reagent (HRP) (ab131366; 1:2,000) were purchased from Abcam. Anti-β-actin (AC026; 1:8,000), anti-β-Tubulin (AC021; 1:8000), anti-Cath A (A5503; 1:1000), anti-p62 (A19700; 1:20,000), HRP-conjugated Goat anti-Mouse IgG (H + L) (AS003; 1:8000) and HRP-conjugated Goat anti-Rabbit IgG (H + L) (AS014; 1:8000) were purchased from ABclonal Technology. Anti-GAPDH (60004-1-Ig; 1:50,000), anti-MST4 (10847-1-AP; 1:1000), anti-LAMP1 (21997-1-AP; 1:1000), anti-HSC70 (10654-1-AP; 1:3000), anti-MEF2D (14353-1-AP; 1:1000), anti-CD44 (15675-1-AP; 1:20,000), anti-ATG4B (15131-1-AP; 1:1000), anti-ATG5 (10181-2-AP; 1:1000), anti-COXIV (11242-1-AP; 1:5000), anti-GFP-tag (66002-1-Ig; 1:20,000) and anti-His-tag (66005-1-Ig; 1:5000) were purchased from Proteintech. Anti-TET1 (40142S; 1:1000), anti-TET2 (45010S; 1:1000), anti-TET3 (99980S; 1:1000), anti-cGAS (79978S; 1:1000), anti-STING (13647S; 1:1000), anti-phospho-STING (Ser366) (19781S; 1:1000), anti-TBK1 (3504S; 1:1000), anti-phospho-TBK1 (Ser172) (5483S; 1:1000), anti-TSC1 (6935S; 1:1000), anti-TSC2 (3990S; 1:1000), anti-4EBP1 (9644S; 1:1000), anti-phospho-4EBP1 (Thr37/46) (2855S; 1:1000), anti-P70S6K (34475S; 1:1000), anti-phospho-P70S6K (Thr389) (9234S; 1:1000) and anti-LC3B (3868S; 1:1000) were purchased from Cell Signaling Technology. Anti-Flag-tag (GNI4110-FG; 1:2000) and anti-Myc-tag (GNI4110-MC; 1:2000) were purchased from GNI. Anti-HA-tag (901515; 1:2000) was purchased from BioLegend. Anti-p-Ser/Thr (612549; 1:1000) was purchased from BD Biosciences. Anti-Cyclophilin A (R381723; 1:1000), anti-HSP40 (250684; 1:1000), anti-HSP90 (R24635; 1:1000), anti-ALDH1A3 (670057; 1:1000) and anti-Tuj1 (beta III Tubulin) (R23620; 1:1000) were purchased from ZENBIO. Anti-LAMP2A pT136 (1:1000) was produced in this study.

The antibodies for immunoprecipitation (IP) were provided as follows: anti-LAMP2A (ab125068; 1:60) was purchased from Abcam. Anti-GFP-tag (66002-1-Ig; 0.5 μg) was purchased from Proteintech. Anti-CathA (A5503; 0.5 μg), Rabbit Control IgG (AC005; 0.5 μg) and Mouse Control IgG (AC011; 0.5 μg) were purchased from ABclonal Technology.

The following antibodies were used in immunofluorescent (IF) staining: anti-LAMP2A (ab125068; 1:500), anti-CD8α (ab237709; 1:100) and anti-PD-L1 (ab213524; 1:500) were purchased from Abcam. Anti-Flag-tag (66008-4-Ig; 1:2000), anti-GZMB (13588-1-AP; 1:200), anti-TSC1 (29906-1-AP; 1:400), anti-TSC2 (24601-1-AP; 1:400), anti-TET3 (22612-1-AP; 1:400), anti-HSC70 (10654-1-AP; 1:400) and anti-Myc-tag (60003-2-Ig; 1:500) were purchased from Proteintech. Anti-LAMP1 (sc-20011; 1:400), anti-CD8 (sc-1177; 1:200) and anti-FoxP3 (sc-53876; 1:200) were purchased from Santa Cruz Biotechnology. Anti-CD4 (A26036PM; 1:200) was purchased from ABclonal Technology. Anti-LC3B (3868S; 1:1000) and anti-phospho-P70S6K (Thr389) (9234S; 1:400) were purchased from Cell Signaling Technology. Goat anti-Rabbit IgG (H + L) Cross-Adsorbed Secondary Antibody Alexa Fluor™ 488 (A-11008; 1:500), Goat anti-Rabbit IgG (H + L) Cross-Adsorbed Secondary Antibody Alexa Fluor™ 594 (A-11012; 1:500), Goat anti-Mouse IgG (H + L) Cross-Adsorbed Secondary Antibody Alexa Fluor™ 488 (A-11001; 1:500), Goat anti-Mouse IgG (H + L) Cross-Adsorbed Secondary Antibody Alexa Fluor™ 594 (A-11005; 1:500) and Donkey anti-Mouse IgG (H + L) Cross-Adsorbed Secondary Antibody Alexa Fluor™ 647 (A-31571; 1:500) were purchased from Invitrogen. Anti-LAMP2A pT136 (1:400) was produced in this study.

The following antibodies were used in immunohistochemistry (IHC): anti-LAMP2A pT136 (1:100) was produced in this study. Anti-MST4 (10847-1-AP; 1:100) was purchased from Proteintech. Anti-TET3 (99980S; 1:100), anti-TSC1(6935S; 1:100) and anti-TSC2 (3990S; 1:100) were purchased from Cell Signaling Technology.

The following antibodies were used in flow cytometry (FC): Pharmingen™ PE-Cy™7 Rat anti-mouse IFN-γ (557649), Horizon™ BV711 Rat anti-mouse TNF (563944) were purchased from BD Biosciences. FITC mouse anti-human CD8 (980908), FITC anti-mouse CD45 (103107), PE anti-human IFN-γ (502509), PE anti-mouse CD103 (121405), PE anti-mouse FOXP3 (126403), PE/Dazzle™ 594 anti-mouse CD366 (119747), PE/Dazzle™ 594 anti-mouse Ly-6C (128044), PE/Cyanine7 anti-human TNF-α Antibody (502930), Brilliant Violet 421™ anti-mouse Ly-6G (127627), Brilliant Violet 510™ anti-mouse CD3 Antibody (100233), Brilliant Violet 605™ anti-mouse/human CD11b (101237), Brilliant Violet 605™ anti-mouse CD152 (106323), Brilliant Violet 650™ anti-mouse CD69 (104541), Brilliant Violet 650™ anti-mouse CD223 (125227), Brilliant Violet 785™ anti-mouse CD25 (102051), PerCP/Cyanine5.5 anti-mouse CD8a (100734), Alexa Fluor® 647 anti-human/mouse Granzyme B (515406) and Pacific Blue™ anti-mouse CD4 (100427) were purchased from Biolegend. These antibodies used for FC were diluted at a ratio of 0.25 μg per 10^6 cells.

Cell lines and cell culture

The HEK293T, LN229, T98G and HeLa cell lines used in this study were obtained from American Type Culture Collection (ATCC). Glioma cell lines U87, U251, GL261 and CT-2A were generously provided by Dr. Chunsheng Kang at Tianjin Medical University General Hospital[84,85]. The MRC-5 cell line was provided by Professor Ningshao Xia at Xiamen University. All cell lines were maintained in DMEM (11965092; Invitrogen) supplemented with 10% Fetal Bovine Serum (FBS)

(A0500-3011; Cegrogen) and 1% penicillin/streptomycin (15140122; Invitrogen). The GSC M83 cell line was provided by Dr. Haizhong Feng at Shanghai Jiao Tong University[86], whereas GSC 23, 456 and 28 cell lines were obtained from Dr. Nu Zhang at the First Affiliated Hospital of Sun Yat-sen University as previously documented[87,88]. GSCs were cultured as non-adherent spheroids in a serum-free defined medium comprising DMEM/F12 (C11330500BT; Gibco), supplemented with 2% B27 (12587010; Invitrogen), 1% penicillin and streptomycin (15140122; Invitrogen), 5 mg/ml heparin (9041-08-1; Sigma-Aldrich) and growth factors EGF (20 ng/mL; AF-100-15; Peprotech) and FGF (20 ng/mL; 100-18B; Peprotech). The DGC M83, 23 and 456 cell lines were derived from GSC M83, 23 and 456 cell lines following differentiation induced by DMEM medium supplemented with 10% FBS and 1% penicillin/streptomycin, incubated at 37 °C with 5% CO_2 for two days. All cell lines tested negative for mycoplasma contamination.

Animal studies

Male athymic (homozygous Foxn1nu BALB/c nude) mice and C57BL/6 mice at 4-5 weeks of age were purchased from Guangdong Yaokang Biotechnology Co., Ltd. Five mice were grouped in each cage and housed under specific-pathogen-free (SPF) conditions with a standardized 12 h light/dark cycle. The ambient temperature was maintained at 21–23 °C with a relative humidity of 50%.

For the tumorigenicity studies, 5×10^4 GSC M83 or 5×10^5 GSC 23 cells or 1×10^5 GL261 cells were injected intracranially into BALB/c Nude mice. 1×10^5 CT-2A or GL261 cells were injected intracranially into C57BL/6 mice. Tumor cells were injected into the brain of individual mice, using the following coordinates from bregma: 2.5 mm lateral, 1.5 mm anterior, and 3.0 mm deep from the skull. All mice were subjected to daily observation to assess the emergence of neurological symptoms indicative of significant tumor progression. The mice were humanely euthanized between 2 to 10 weeks post-implantation, and their brains were subsequently extracted. Each brain was carefully excised and preserved in an optimum cutting temperature (OCT) compound (Sakura Finetek), then stored at -80 °C. Brains containing tumors were sliced into 10 µm thick sections utilizing a cryostat (Leica CM1950). The entire brain was sectioned coronally from the anterior to the posterior regions. Every fifth section from each tumor-infiltrated brain underwent hematoxylin and eosin staining to identify the spatial distribution of the tumors from inception to termination. These images of sections were stained with hematoxylin and eosin obtained from MshOt microscopy system. After thorough evaluation, the section exhibiting the maximum cross-sectional area of the tumor for each xenograft was selected for volumetric assessment. Tumor volume was calculated utilizing the formula $V = ab^2/2$, where a and b (with $a > b$) represent the tumor's length and width, respectively.

For in vivo therapeutic assays, the C57BL/6 mice stereotactically transplanted with CT-2A or GL261 cells were randomized into each treatment group. For depletion of $CD8^+$ cells, mice received intraperitoneal administrations of CD8α monoclonal antibody (10 mg/kg; BE0061; Bio X Cell) or IgG2b (10 mg/kg; BE0086; Bio X Cell) every three days from one week after implantation. For immune checkpoint blockade, mice received intracranial administrations of the anti-programmed cell death protein 1 (PD-1) monoclonal antibody (10 mg/kg; BE0146; Bio X cell) or IgG2a (10 mg/kg; BE0085; Bio X Cell) on the 8th, 12th, 16th, and 20th day after implantation. The radiation groups received 2 Gy of radiation daily for five days, starting two weeks post-transplantation alongside treatment. To evaluate the impact of PPD treatment, mice received 6 mg/kg PPD or DMSO intragastrically for seven consecutive days starting from the 10th day after implantation. The mice were observed daily for neurological symptoms related to tumor growth, and maintained until symptoms appeared, such as hunching, weight loss, decreased food intake and lethargy. To track tumor growth following radiation or drug treatment, each mouse received an injection of D-luciferin potassium salt at a dosage of 150 mg/kg, and tumor growth was assessed using the IVIS Lumina imaging station (Caliper Life Sciences).

Bioinformatic analysis of LAMP2A correlated pathways

We obtained the RNA-seq dataset GSE181556 from NCBI's Gene Expression Omnibus, specifically examining control and sh-LAMP2A samples[17]. Differentially expressed genes (DEGs) were screened based on criteria of a fold change ≥ 2 and a false discovery rate (FDR) < 0.01. Enrichment analysis of biological pathways was conducted using clusterProfiler, with pathways enriched at $p < 0.05$ considered significantly correlated with the DEG set. Additionally, proteome data was accessed from the ProteomeXchange Consortium, utilizing the dataset identifier PXD027069. Significantly differential proteins ($p < 0.05$) with a ratio > 1.5 in either direction were analyzed using DAVID to characterize their involved biological pathways, with pathways enriched at $p < 0.05$ deemed significantly correlated with the set of differential proteins.

Bioinformatic analysis of *CGAS/STING*

Firstly, we acquired GSE181556 dataset and utilized the normalized expression matrix to analyze signaling pathways correlated to LAMP2A through Gene Set Enrichment Analysis (GSEA)[89]. Subsequently, DNMIVD[90–92] was used to examine the correlation between *CGAS/STING* levels and the mean DNA methylation of the *CGAS/STING*'s promoter, respectively. Furthermore, the expression correlations between CGAS/STING and TETs/DNMTs were analyzed using Pearson's correlation based on TCGA (https://xena.ucsc.edu/)[93] and CGGA[94] datasets.

Bioinformatics analysis of immune infiltration based on CMA score

As previously described[95], to quantify the activity of the CMA pathway within individual cells, a CMA score was calculated based on the expression levels of a predefined set of CMA-associated genes to reflect the coordinated expression changes associated with CMA activity in each cell. Briefly, each component in the CMA network was assigned a weight. Since LAMP2A is the rate-limiting factor, it received a weight of 2, while all other elements were assigned a weight of 1. Then, each element was assigned a directional score (+1 or -1) based on its known regulatory effect on CMA activity. The final CMA score was computed as a weighted, direction-adjusted average of the expression levels across all network components. TCGA-GBM counts expression data were used to calculate the CMA score. Immune infiltration data for TCGA-GBM were obtained from TIMER and TISIDB. GSVA R package (version 1.52.3) was used to calculated the MDSC infiltration (include CD33, ITGAM, and CD15). The relationship between CMA scores and immune infiltration levels was assessed using Spearman's correlation analysis and Pearson's correlation analysis. Statistical significance was defined as $p < 0.05$, and the strength of linear associations was interpreted based on the resulting Spearman's correlation coefficients or Pearson's correlation coefficients.

Plasmid construction

The open reading frames (ORFs) for MST4 and LAMP2A were cloned into the pCDH-CMV-MCS-EF1-Puro vector, resulting in the construction of pCDH-HA-MST4, pCDH-Flag-MST4 and pCDH-Flag-LAMP2A. The ORF of TSC1/2 and TET1/2/3, along with their variants, were subcloned into the pCMV6 vector, incorporating a sequence that encodes a N-Myc epitope. Site-directed mutagenesis was performed using the Q5® Site-Directed Mutagenesis Kit (E0554; NEB), adhering to the manufacturer's protocols.

Human cDNAs corresponding to LAMP2A and its variants were amplified via PCR and subsequently sub-cloned into the pET-28a vector for expression in *E. coli*.

The pLKO.1 lentiviral shRNA constructs targeting LAMP2A, MST4, HSC70, TSC1/2, TET1/2/3, cGAS, ATG4B and ATG5 were designed in accordance with the protocol available on the Addgene website (https://www.addgene.org/protocols/plko/). All target sequences shRNAs are listed in Supplementary Table 2.

To knock out *STK26*, the target sequence of gRNA was designed by the CRIStick online website (https://portals.broadinstitute.org/gppx/crispick/public). The synthesized primer containing a 20 bp target sequence (5′-CTCGCCGGTGGCTGTCCAAG-3′ or 5′-GGGCGGTGGTTCAGCACTGG-3′) was annealed and inserted into lenti-CRISPR-v2 using T4 ligase (FL101; TransGen Biotech).

All primers used for plasmid construction were synthesized by Sangon Biotech (Shanghai) Co., Ltd., and were listed in Supplementary Table 3.

All resulting cDNA constructs and mutants were validated for accuracy through DNA sequencing.

Lentiviral production and infection

Lentiviral vectors harboring shRNAs, or full-length cDNAs for MST4, LAMP2A, and their respective mutants were introduced into HEK293T cells utilizing Lipofectamine 2000 (Life Technologies), following the manufacturer's protocols. In gene rescue assays, shRNAs designed to target the 3′ untranslated regions of MST4, LAMP2A, TSC1/2, and TET3 were employed for knockdown purposes. The lentiviral supernatants were harvested at 48 and 72 h post-transfection and subsequently used to infect recipient cells in the presence of polybrene (6 mg/mL). Following a 72-hour transduction period, the cells underwent selection with puromycin at a concentration of 1 mg/mL for four days.

Immunoblot (IB) analysis

Cells were lysed using RIPA buffer (E121-01; GenStar) supplemented with protease and phosphatase inhibitors on ice, followed by centrifugation at 15,000 × *g* for 15 minutes at 4 °C. The resultant supernatant was utilized to prepare the protein sample for SDS-PAGE analysis. Proteins were subsequently transferred from the gel to a polyvinylidene fluoride (PVDF) membrane (IPVH00010; Millipore) in a transfer buffer containing 25 mM Tris and 192 mM glycine. The membranes were blocked with 5% fat-free milk at 37 °C for 2 h and then incubated with the primary antibody at 4 °C overnight. After wash with TBST (TBS with 0.1% Tween-20), the membranes were treated with the appropriate secondary antibodies. Detection was performed using an enhanced chemiluminescence (ECL) (GCP1001-500-ES; GENECYCLER) assay according to the manufacturer's protocol.

The degradation rate of LAMP2A in isolated lysosomes was evaluated using IB with a specific antibody against LAMP2A, following established methods[13]. In summary, the lysosomes were incubated at 0 °C for 10 min with or without lysosome protease inhibitor cocktail (PI) consisting of: 10 μM leupeptin (targeting serine/cysteine proteases), 10 μM AEBSF (serine protease inhibitor), 1 μM pepstatin A (aspartic protease inhibitor), and 100 μM EDTA (metalloprotease inhibitor). At various time points, samples were taken for SDS-PAGE and immunoblotting analysis of LAMP2A.

Immunoprecipitation (IP)

Cells were lysed using IP lysis buffer (87787; ThermoFisher Scientific) supplemented with protease and phosphatase inhibitors, incubated on ice for 15 min, and then centrifuged at 15,000 × *g* for 15 min at 4 °C to eliminate cellular debris. Following a pre-clearing step with protein G/protein A-agarose beads (IP10; Sigma-Aldrich), the supernatant was then immunoprecipitated with anti-DYKDDDDK (Flag) G1 Affinity Resin (L00432; GenScript), anti-Myc affinity gel (GNI4510-MC; GNI), anti-HA-magnetic-beads (B26202; Bimake), or agarose-immobilized anti-LAMP2A, anti-Cath A, anti-GFP-tag, Mouse Control IgG or Rabbit Control IgG at 4 °C overnight.

Native gel electrophoresis

Lysosomal membranes were isolated according to established protocols[96], and subjected to continuous native polyacrylamide gel electrophoresis (6% natural polyacrylamide gel devoid of SDS) in a non-reducing loading buffer without boiling, as outlined by Rodriguez-Navarro JA. et al.[97]. Following transfer to PVDF membranes, the LAMP2Acontaining complexes were identified using an anti-LAMP2A antibody.

Immunofluorescent (IF) staining

For immunofluorescent staining of cultured cells, cells were fixed using 4% paraformaldehyde for 15 min, followed by permeabilization with 0.3% Triton X-100, and subsequently blocked with 5% BSA for 2 h. Primary antibodies were applied and incubated overnight at 4 °C. After wash with PBS, the cells were incubated with Alexa Fluor™ 488, 594 or 647 conjugated secondary antibodies in the dark. Following additional wash with PBS, the cells were treated with DAPI (AR1176; BOSTER). After mounting, the samples were examined using an inverted microscope fitted with a Nikon digital camera, and quantitative analysis was conducted using Image J software.

For immunofluorescent staining of tissue sections, the sections were fixed similarly to the cultured cells, then subjected to permeabilization with 0.5% PBST (PBS supplemented with 0.5% Triton X-100) for 30 min and blocked with 5% BSA for 2 h. Sections were incubated overnight at 4 °C with primary antibodies. The subsequent incubation with secondary antibodies and DAPI followed the same protocol as for cultured cells. Ultimately, the sections were analyzed using an inverted microscope equipped with a Nikon digital camera, with statistical analysis performed using Image J software.

Quantitative real-time PCR (qRT-PCR)

Total RNA was extracted from cells using TRIzol (R1000; Lablead) and reversely transcribed into cDNA using Hifair III Reverse Transcriptase (11297ES09; YEASEN). The cDNA products were analyzed via qRT-PCR with SYBR Green PCR Master Mix (11201ES08; YEASEN). Detailed information about the primer sequences utilized can be found in Supplementary Table 4.

Flow cytometric analysis

Single-cell suspensions were prepared by enzymatically dissociating isolated mouse glioma tissues using Collagenase IV (HY-E70005D; MCE) and DNase I (HY-108882; MCE). Following the lysis of erythrocytes with a lysis buffer (G2015; Servicebio), the cells were activated with the BD Pharmingen™ Leukocyte Activation Cocktail supplemented with BD GolgiPlug™ (550583; BD Biosciences) at 37 °C in a 5% CO_2 atmosphere for a duration of 4 h. After a 15 min incubation on ice, shielded from light, with the Zombie NIR™ Fixable Viability Kit (423105; BioLegend), the surface marker staining solution (including antibodies such as CD45, CD3, CD4, CD8, etc.) was prepared according to the specified concentrations. The cells were incubated with the staining solution on ice in the dark for 30 min. Following this, the cells were fixed and permeabilized using BD Cytofix/Cytoperm™ Solution (554722; BD Biosciences) before undergoing intracellular target staining (e.g., TNF-α, IFN-γ). Flow cytometry data were collected using a BD FACSymphony™ A1 instrument and subsequently analyzed utilizing FlowJo v10 software.

Apoptosis detection

In accordance with the manufacturer's specifications, cellular apoptosis was assessed utilizing the APC Annexin V Apoptosis Detection Kit in conjunction with Propidium Iodide (PI) (640932; Biolegend). Cells underwent two washes with cold BioLegend Cell Staining Buffer (420201; Biolegend) and were then resuspended in Annexin V Binding Buffer (422201; Biolegend) at a density of 0.25–1.0 × 10^7 cells/mL. A volume of 100 μL of the cell suspension was pipetted into a 5 mL test tube, followed by the introduction of 5 μL of fluorochrome-conjugated Annexin V. The cells were subsequently stained with propidium iodide as a viability marker, gently vortexed, and incubated for 15 min at room temperature (25 °C) in the absence of light. Post-incubation, 400 μL of Annexin V Binding Buffer was added to each tube, and the samples were analyzed via flow cytometry.

$CD8^+$ T cell preparation and co-culture

$CD8^+$ T lymphocytes were isolated from peripheral blood mononuclear cells of GBM patients utilizing the Human $CD8^+$ T Cell Enrichment Cocktail kit (15023; STEMCELL Technologies). The purified $CD8^+$ T cells were cultured in X-VIVO 15 medium (04-418Q; Lonza) supplemented with 10 ng/mL of IL-2 (200-02-50UG; PeproTech) and subsequently activated using human anti-CD3/CD28 Dynabeads (11161D; Thermo Fisher) for a period of 48 to 72 h. Following activation, the T cells and GSCs were enumerated and introduced into the GSC culture system at a 1:5 ratio for a 24 h co-culture at 37 °C with 5% CO_2, after which flow cytometric analysis was performed.

Identification of phosphorylation sites by LC-MS/MS analysis

To identify LAMP2A phosphorylation, Flag-LAMP2A was immunoprecipitated from HEK293T cells stably expressing exogenous HA-MST4 and Flag-LAMP2A using anti-DYKDDDDK (Flag) G1 Affinity Resin. The resulting immune complexes were subjected to SDS-PAGE for resolution and subsequently stained with Coomassie brilliant blue. Gel segments containing LAMP2A were dehydrated in acetonitrile, dried under a speed vacuum, and digested with trypsin. The resulting peptides were extracted from the polyacrylamide matrix and concentrated for subsequent liquid chromatography-mass spectrometry (LC-MS) analysis at the Core Facility for Biomedical Sciences at Xiamen University. The mass spectrometry dataset has been deposited in the PRIDE repository (Accession unmber: PXD060464).

CMA activity detection by KFERQ puncta

As previously described[37], CMA activity was detected by the photoactivable reporter, pSIN-PAmCherry-KFERQ-NE (Addgene). GSC and non-GSC cell lines expressing PAmCherry-KFERQ-NE were photoactivated by exposure to 405/20 nm LED array (Norlux) for 10 min. Alterations in the cellular pattern of the reporter were examined utilizing confocal microscopy (Zeiss LSM980 or Nikon A1R), and image quantification was performed with Image J software. Enhanced CMA activity was evidenced by an increase in the number of red fluorescent puncta per cell.

In vitro cell proliferation assay

GSC spheres were dissociated into individual cells, and the viable cells (negative for Trypan Blue) were enumerated using a hemocytometer. The cells were subsequently plated in a 24-well plate with 1 mL of culture medium at a density of 5000 cells per well, and viable cell counts for each well were performed daily for five consecutive days using a hemocytometer.

Limited dilution assays for GSCs

Dissociated cells harvested from glioma spheres were plated in 96-well plates at densities of 1, 5, 10, 20 or 50 for GSC M83, 456 and 23 cells. After 7 days, tumor sphere formation was assessed from each well. The frequency of stem cells was determined utilizing extreme limiting dilution analysis (https://bioinf.wehi.edu.au/software/elda/).

In vitro kinase assay

The pCDH-Flag-MST4 expression vector was introduced into HEK293T cells via lipofectamine 2000 (Thermo Fisher Scientific). Following a 48-hour incubation, the cells were lysed using a lysis buffer supplemented with protease and phosphatase inhibitors. The Flag-MST4 protein from the cell lysates was subsequently immunoprecipitated using anti-DYKDDDDK (Flag) G1 Affinity Resin at 4 °C overnight. The isolated MST4 proteins were then re-suspended in a mixture containing 1 × kinase buffer (9802S; Cell Signaling Technology), 200 μM ATP (9804S; Cell Signaling Technology), and purified His-tagged LAMP2A variants (WT, T40A, S97A, T136A, T40A/S97A, T40A/T136A, S97A/T136A, T40A/S97A/T136A). The kinase reaction was conducted for one hour at 30 °C and subsequently quenched with 20 mL of 3 × SDS sample buffer. Each sample was then subjected to boiling for 10 minutes at 100 °C after the addition of loading buffer, followed by SDS-PAGE and immunoblotting analysis utilizing the specified antibodies.

Lysosomes isolation

Lysosomes were purified from cells using a lysosome isolation kit from Biovision (K235-50). According to the protocol, 2×10^7 cells were washed with PBS at 100 × g for 1 min and resuspended in 500 μL lysosome isolation buffer for 2 minutes. The suspension was homogenized with a Dounce homogenizer for 40 times. Then the homogenate was transferred to the tube containing 500 μL lysosome enrichment buffer and mixed, and centrifuged at 500 × *g* for 10 min. The supernatant was centrifuged at a density gradient of 20,000 × *g* for 2 h. The lysosome precipitate was collected with appropriate volumes of PBS, and centrifuged at 18,000 × *g* for 30 minutes. All steps were conducted on ice or maintained at a temperature of 4 °C. The extracted lysosomes were absence of any cytoplasmic or mitochondrial components by IB detection of markers.

In vitro lysosome binding and uptake assay

According to the previously reported study[98], incubating purified His-tagged GAPDH with intact lysosomes from GSCs, pre-treated or not with lysosome protease inhibitor cocktai (PI) that inhibit lysosomal proteolytic activity, facilitates the quantification of substrate binding and translocation into the lysosomal lumen. In untreated lysosomes, internalized proteins are rapidly degraded, allowing only membrane-bound proteins to be detected. NH_4Cl, a lysosomotropic compound, neutralizes lysosomal pH, which may lead to lysosomal impairment[99]. For CMA activity assays, PI was used instead of leupeptin/NH_4Cl to specifically inhibit lysosomal proteases while minimizing interference with CMA machinery. Following a 20 min incubation with recombinant protein in 20 mM MOPS, 0.3 M sucrose buffer at 37 °C, samples were centrifuged at 25,000 × *g* for 5 min at 4 °C. The resultant pellets were washed with the incubation buffer, resuspended, denatured in sample buffer at 95 °C for 5 min, and analyzed via SDS-PAGE and immunoblotting. Proteins associated with lysosomes untreated with PI represented the protein binding to lysosomes, and uptake was calculated by subtracting the binding proteins from the total proteins in lysosomes treated with PI[100]. Quantification of protein band intensities on the immunoblots was performed using Image J software.

For other CMA substrates (TSC1, TSC2, and TET3), Myc-TSC1/2 and -TET3 were overexpressed in HEK293T cells, followed by IP using anti-Myc affinity gel and subsequent elution with 150 μg/mL Myc competitive peptides (P9805; Beyotime Biotechnology). The purified Myc-tagged substrates were then incubated with lysosomes isolated from 293 T cells in reaction buffer (20 mM MOPS, 0.3 M sucrose) with or without PI at 37 °C for 20 min. Following incubation, lysosomes were isolated via centrifugation and analyzed using SDS-PAGE and immunoblotting. The protein found in untreated lysosomes indicated binding, while the uptake was determined by subtracting the protein levels in lysosomes treated with protease inhibitors from those in untreated lysosomes[21].

Senescence-associated beta-Galactosidase (SA-β-gal) staining

SA-β-gal activity was assessed using a Cellular Senescence β-Galactosidase Staining Kit (C0602; Beyotime Biotechnology). Cells were seeded in 6-well plates containing complete culture medium and cultured for 48 hours. Following fixation for 15 min, cells were washed three times with PBS. The fixed cells were then incubated with β-galactosidase staining solution at 37 °C overnight in a CO_2-free incubator. Images of stained cells were obtained from MshOt microscopy system and quantitative analysis was performed using Image J software.

IHC analysis of clinical glioma specimens

Research involving patient specimens received partial approval from the institutional review boards at Union Hospital, Tongji Medical College, Huazhong University of Science and Technology (UHHUST), and was carried out in compliance with Xiamen University regulations. The samples were collected under the clinical protocol No. UHCT-IEC-SOP-016-03-01, which was sanctioned by the UHHUST institutional review board. Signed informed consent was obtained from all participating individuals prior to participation in the study. IHC staining was performed a cohort of 83 patient glioma samples with the specified antibodies. Images of IHC sections were obtained by MshOt microscopy system and were quantitatively scored based on the percentage of positively stained cells and staining intensity, following established protocols[101,102]. Scoring was: 0 for 0% positive tumor cells, 1 for 0 - 1%, 2 for 2 - 10%, 3 for 11 - 30%, 4 for 31 - 70%, and 5 for 71 - 100%. Staining intensity was rated from 0 to 3, with 0 as negative, 1 weak, 2 moderate, and 3 strong. The total score, from 0 to 8, combined the proportion and intensity scores. These scores were compared with overall survival, defined as the time from diagnosis to death or last follow-up. Kaplan-Meier plots for overall survival rates of GBM patients were generated, classifying them into high (score 4 - 8) and low (score 0 - 3) expression groups of the indicated protein. Due to antibody sensitivity variations and glioma tumor sample heterogeneity, the number of samples showing high or low expression of specific proteins varies across the graphs, even with the same scoring criteria.

To investigate the prognostic significance of MST4, LAMP2A pT136, TET3, and TSC1/2 protein expression, we employed block randomization stratified by age, sex, and WHO grade to ensure balanced distribution of potential confounders across experimental cohorts. Kaplan-Meier survival curves were generated comparing overall survival between expression groups, with rigorous control for tumor heterogeneity and antibody performance variations. Comorbidities including cephalalgia ($n = 20$), epilepsy ($n = 3$), and seizure ($n = 5$) were documented in Supplementary Dataset, but excluded from primary analysis to minimize confounding effects. This methodological approach ensured the observed survival correlations primarily reflected the biological impact of target protein expression patterns.

PNGase F treatment

LAMP2A protein was immunoprecipitated using an anti-LAMP2A antibody from GSC M83, along with their corresponding DGCs. A total of 60 µL of denaturing buffer (10 mM Tris-HCl, pH 6.8, 8 mM dithiothreitol, and 0.1% SDS) was added to the washed agarose resin, which was then heated to 100 °C for 5 min. After brief centrifugation, 20 µL of the eluted material was combined with 30 µL of reaction buffer (80 mM sodium phosphate, pH 7.5, and 1.6% NP-40), with or without 8,000 U/mL PNGase F (P0704; New England BioLabs), and incubated at 37 °C for 1 h. Finally, the reactions were analyzed by IB.

Lectin blotting

The protein samples were subjected for SDS-PAGE analysis and subsequently transferred from the gel to a PVDF membrane in the transfer buffer. The membranes were blocked with 5% BSA at 37 °C for 30 min and then incubated with biotin-labeled Concanavalin A (ConA) (B-1005-5; Vector Laboratories) and HRP-conjugated streptavidin (SE068; Solarbio LIFE SCIENCES). After wash with PBST (PBS supplemented with 0.05% Tween 20), the membranes were performed using an ECL assay.

Antibody production

Polyclonal antibodies against the phosphorylated T136 residue of LAMP2A were produced in murine hosts via immunization with a synthetic phosphopeptide mimicking the sequence adjacent to the T136 site of human LAMP2A (AEDKGIL(p-T) VDELLAIC). Antisera titers were quantified to be approximately 1:10,000 through enzyme-linked immunosorbent assay (ELISA). IgG fractions were subsequently purified using protein A-Sepharose (Bio-Rad). These antibodies underwent stringent specificity assessment via IB, IF and IHC, utilizing both modified and unmodified peptide controls. Non-specific IgG served as a negative control.

Quantification and statistical analysis

Statistical analysis was carried out using Microsoft Excel 2021, GraphPad Prism version 8, R 4.1.3 and RStudio 2023.12.0 + 369 for Windows. The analysis included Student's T-test (two-tailed), one-way ANOVA with Tukey's multiple comparisons test or Dunnett's multiple comparisons test and two-way ANOVA with Bonferroni's multiple comparisons test. The Kaplan-Meier survival curves and log-rank test were used to determine the differences in survival rates between two groups. Cox proportional hazards model was employed to perform univariate and multivariate analysis. All grouped data are presented as mean ± S.E.M., unless otherwise stated. $p < 0.05$ was considered statistically significant.

Ethics statement

Our research complies with all relevant ethical regulations of Xiamen University and Huazhong University of Science and Technology. All animal protocols were approved by the Animal Research Ethics Committee of Xiamen University. The animal experiments were performed in accordance with the Guidelines for the Care and Use of Laboratory Animals and received approval from the Institutional Animal Care and Use Committee (IACUC) at Xiamen University. The Animal Ethics Committee of Xiamen University allows a maximum tumor diameter of 15 mm, and all tumors in our experiments adhered to this limit. None exceeded this size. The collection and use of clinical materials were approved by the Medical Research Ethics Committee of Huazhong University of Science and Technology and Xiamen University.

Reporting summary

Further information on research design is available in the Nature Portfolio Reporting Summary linked to this article.

Data availability

Mass spectrometry proteomics data have been deposited to the ProteomeXchange Consortium (http://www.proteomexchange.org/) via the PRIDE partner repository with the dataset identifiers PXD060464. The RNA-seq analysis utilized publicly available data from GSE181556. Proteomic comparisons were derived from dataset PXD027069. Both datasets originate from a prior study by Auzmendi-Iriarte et al.[17]. For clinical datasets, we have ensured that the data availability statement aligns with the policy outlined at (https://www.nature.com/nature-research/editorial-policies/reporting-standards#availability-of-data). This statement has been uploaded and submitted as supplementary material. All data supporting the key findings of this study are available within the article, the supplementary information, and the source data file. Source data are available within this publication. For additional inquiries, please contact the corresponding author, Tianzhi Huang (huangtianzhi@xmu.edu.cn). Source data are provided with this paper.

References

1. Chen, J., McKay, R. M. & Parada, L. F. Malignant Glioma: Lessons from Genomics, Mouse Models, and Stem Cells. *Cell* **149**, 36–47 (2012).
2. Ostrom, Q. T. et al. CBTRUS Statistical Report: Primary Brain and Other Central Nervous System Tumors Diagnosed in the United States in 2009–2013. *Neuro-Oncol.* **18**, v1–v75 (2016).

3. Reardon, D. A. et al. Effect of Nivolumab vs Bevacizumab in Patients With Recurrent Glioblastoma: The CheckMate 143 Phase 3 Randomized Clinical Trial. *JAMA Oncology* **6**, (2020).
4. Gimple, R. C., Bhargava, S., Dixit, D. & Rich, J. N. Glioblastoma stem cells: lessons from the tumor hierarchy in a lethal cancer. *Genes Dev.* **33**, 591–609 (2019).
5. Bao, S. et al. Glioma stem cells promote radioresistance by preferential activation of the DNA damage response. *Nature* **444**, 756–760 (2006).
6. Chen, J. et al. A restricted cell population propagates glioblastoma growth after chemotherapy. *Nature* **488**, 522–526 (2012).
7. Zhong, J. et al. Circular EZH2-encoded EZH2-92aa mediates immune evasion in glioblastoma via inhibition of surface NKG2D ligands. *Nat. Commun.* **13**, 4795 (2022).
8. Maria Cuervo, A. Autophagy: in sickness and in health. *Trends Cell Biol.* **14**, 70–77 (2004).
9. Debnath, J., Gammoh, N. & Ryan, K. M. Autophagy and autophagy-related pathways in cancer. *Nat. Rev. Mol. Cell Biol.* **24**, 560–575 (2023).
10. Kaushik, S. & Cuervo, A. M. The coming of age of chaperone-mediated autophagy. *Nat. Rev. Mol. Cell Biol.* **19**, 365–381 (2018).
11. Cuervo, A. M. & Wong, E. Chaperone-mediated autophagy: roles in disease and aging. *Cell Res.* **24**, 92–104 (2013).
12. Chiang, H. L., Terlecky, S. R., Plant, C. P. & Dice, J. F. A role for a 70-kilodalton heat shock protein in lysosomal degradation of intracellular proteins. *Science* **246**, 382–385 (1989).
13. Cuervo, A. M. & Dice, J. F. Regulation of lamp2a levels in the lysosomal membrane. *Traffic* **1**, 570–583 (2001).
14. Qiao, L. et al. LAMP2A, LAMP2B and LAMP2C: similar structures, divergent roles. *Autophagy* **19**, 2837–2852 (2023).
15. Cuervo, A. M. & Dice, J. F. A receptor for the selective uptake and degradation of proteins by lysosomes. *Science* **273**, 501–503 (1996).
16. Park, C., Suh, Y. & Cuervo, A. M. Regulated degradation of Chk1 by chaperone-mediated autophagy in response to DNA damage. *Nat. Commun.* **6**, 6823 (2015).
17. Auzmendi-Iriarte, J. et al. Chaperone-Mediated Autophagy Controls Proteomic and Transcriptomic Pathways to Maintain Glioma Stem Cell Activity. *Cancer Res.* **82**, 1283–1297 (2022).
18. Valdor, R. et al. Chaperone-mediated autophagy regulates T cell responses through targeted degradation of negative regulators of T cell activation. *Nat. Immunol.* **15**, 1046–1054 (2014).
19. Khawaja, R. R. et al. Sex-specific and cell-type-specific changes in chaperone-mediated autophagy across tissues during aging. *Nat. aging* **5**, 691–708 (2025).
20. Reynolds, C. A. et al. Restoration of LAMP2A expression in old mice leads to changes in the T cell compartment that support improved immune function. *Proc. Natl. Acad. Sci. USA* **121**, e2322929121 (2024).
21. Kaushik, S. & Cuervo, A. M. Chaperone-mediated autophagy. *Methods Mol. Biol. (Clifton, NJ)* **445**, 227–244 (2008).
22. Nazio, F., Bordi, M., Cianfanelli, V., Locatelli, F. & Cecconi, F. Autophagy and cancer stem cells: molecular mechanisms and therapeutic applications. *Cell Death Differ.* **26**, 690–702 (2019).
23. Guan, J.-L. et al. Autophagy in stem cells. *Autophagy* **9**, 830–849 (2014).
24. Qian, Z., Lin, C., Espinosa, R., LeBeau, M. & Rosner, M. R. Cloning and Characterization of MST4, a Novel Ste20-like Kinase. *J. Biol. Chem.* **276**, 22439–22445 (2001).
25. Getu, A. A., Zhou, M., Cheng, S.-Y. & Tan, M. The mammalian Sterile 20-like kinase 4 (MST4) signaling in tumor progression: Implications for therapy. *Cancer Lett.* **563**, 216183 (2023).
26. Zhang, H. et al. An MST4-p*β*-CateninThr40 Signaling Axis Controls Intestinal Stem Cell and Tumorigenesis. *Adv. Sci.* **8**, e2004850 (2021).
27. Huang, T. et al. MST4 Phosphorylation of ATG4B Regulates Autophagic Activity, Tumorigenicity, and Radioresistance in Glioblastoma. *Cancer Cell* **32**, 840–855.e848 (2017).
28. Hopfner, K.-P. & Hornung, V. Molecular mechanisms and cellular functions of cGAS–STING signalling. *Nat. Rev. Mol. Cell Biol.* **21**, 501–521 (2020).
29. Civril, F. et al. Structural mechanism of cytosolic DNA sensing by cGAS. *Nature* **498**, 332–337 (2013).
30. Wu, J. et al. Cyclic GMP-AMP is an endogenous second messenger in innate immune signaling by cytosolic DNA. *Science* **339**, 826–830 (2013).
31. Ablasser, A. et al. cGAS produces a 2′-5′-linked cyclic dinucleotide second messenger that activates STING. *Nature* **498**, 380–384 (2013).
32. Zhao, B. et al. A conserved PLPLRT/SD motif of STING mediates the recruitment and activation of TBK1. *Nature* **569**, 718–722 (2019).
33. Corrales, L. & Gajewski, T. F. Molecular Pathways: Targeting the Stimulator of Interferon Genes (STING) in the Immunotherapy of Cancer. *Clin. Cancer Res.* **21**, 4774–4779 (2015).
34. Emily N. C. et al. Antitumor activity of a systemic STING-activating non-nucleotide cGAMP mimetic. *Science* **369**, (2020).
35. Lai, J. et al. Zebularine elevates STING expression and enhances cGAMP cancer immunotherapy in mice. *Mol. Ther.* **29**, 1758–1771 (2021).
36. Lv, H. et al. TET2-mediated tumor cGAS triggers endothelial STING activation to regulate vasculature remodeling and anti-tumor immunity in liver cancer. *Nat. Commun.* **15**, 6 (2024).
37. Koga, H., Martinez-Vicente, M., Macian, F., Verkhusha, V. V. & Cuervo, A. M. A photoconvertible fluorescent reporter to track chaperone-mediated autophagy. *Nat. Commun.* **2**, 386 (2011).
38. Aniento, F., Roche, E., Cuervo, A. M. & Knecht, E. Uptake and degradation of glyceraldehyde-3-phosphate dehydrogenase by rat liver lysosomes. *J. Biol. Chem.* **268**, 10463–10470 (1993).
39. Yang, Q. et al. Regulation of neuronal survival factor MEF2D by chaperone-mediated autophagy. *Science* **323**, 124–127 (2009).
40. Cuervo, A. M. & Dice, J. F. Unique properties of lamp2a compared to other lamp2 isoforms. *J. Cell Sci.* **24**, 4441–4450 (2000).
41. Wilke, S., Krausze, J. & Büssow, K. Crystal structure of the conserved domain of the DC lysosomal associated membrane protein: implications for the lysosomal glycocalyx. *BMC Biol.* **10**, 62 (2012).
42. Cuervo, A. M., Knecht, E., Terlecky, S. R. & Dice, J. F. Activation of a selective pathway of lysosomal proteolysis in rat liver by prolonged starvation. *Am. J. Physiol.* **269**, C1200–C1208 (1995).
43. Cuervo, A. M., Mann, L., Bonten, E. J., d'Azzo, A. & Dice, J. F. Cathepsin A regulates chaperone-mediated autophagy through cleavage of the lysosomal receptor. *EMBO J.* **22**, 47–59 (2002).
44. Li, W. et al. Phosphorylation of LAMP2A by p38 MAPK couples ER stress to chaperone-mediated autophagy. *Nat. Commun.* **8**, 1763 (2017).
45. Wick, W., Blaes, J. & Weiler, M. mTORC 2:1 for chemotherapy sensitization in glioblastoma. *Cancer Discov.* **1**, 475–476 (2011).
46. Katsuno, Y. et al. Chronic TGF-β exposure drives stabilized EMT, tumor stemness, and cancer drug resistance with vulnerability to bitopic mTOR inhibition. *Sci. Signal.* **12**, eaau8544 (2019).
47. Akhavan, D., Cloughesy, T. F. & Mischel, P. S. mTOR signaling in glioblastoma: lessons learned from bench to bedside. *Neuro-Oncol.* **12**, 882–889 (2010).
48. Jun S. et al. Dual blocking of mTor and PI3K elicits a prodifferentiation effect on glioblastoma stem-like cells. *Neuro-oncology* **12**, (2010).
49. Szwed, A., Kim, E. & Jacinto, E. Regulation and metabolic functions of mTORC1 and mTORC2. *Physiological Rev.* **101**, 1371–1426 (2021).
50. Laplante, M. & Sabatini, D. M. mTOR signaling in growth control and disease. *Cell* **149**, 274–293 (2012).

51. Bourdenx, M. et al. Chaperone-mediated autophagy prevents collapse of the neuronal metastable proteome. *Cell* **184**, 2696–2714.e2625 (2021).
52. Schnebert, S. et al. Chaperone-mediated autophagy in fish: A key function amid a changing environment. *Autophagy Rep.* **3**, 2403956 (2024).
53. Zhang, X., Bai, X. C. & Chen, Z. J. Structures and Mechanisms in the cGAS-STING Innate Immunity Pathway. *Immunity* **53**, 43–53 (2020).
54. Konno, H. et al. Suppression of STING signaling through epigenetic silencing and missense mutation impedes DNA damage mediated cytokine production. *Oncogene* **37**, 2037–2051 (2018).
55. Li, D., Chen, J. & Pei, D. The Battle between TET Proteins and DNA Methylation for the Right Cell. *Trends Cell Biol.* **28**, 973–975 (2018).
56. Juste, Y. R. et al. Reciprocal regulation of chaperone-mediated autophagy and the circadian clock. *Nat. Cell Biol.* **23**, 1255–1270 (2021).
57. Gong, Y. et al. Vangl2 limits chaperone-mediated autophagy to balance osteogenic differentiation in mesenchymal stem cells. *Dev. Cell* **56**, 2103–2120.e2109 (2021).
58. Chen, R., Xie, R., Meng, Z., Ma, S. & Guan, K. L. STRIPAK integrates upstream signals to initiate the Hippo kinase cascade. *Nat. Cell Biol.* **21**, 1565–1577 (2019).
59. Eden, M. et al. Mst4, a novel cardiac STRIPAK complex-associated kinase, regulates cardiomyocyte growth and survival and is upregulated in human cardiomyopathy. *J. Biol. Chem.* **300**, 107255 (2024).
60. Madsen, C. D. et al. STRIPAK components determine mode of cancer cell migration and metastasis. *Nat. Cell Biol.* **17**, 68–80 (2014).
61. Bandyopadhyay, U., Kaushik, S., Varticovski, L., Cuervo, A. M. & biology c The chaperone-mediated autophagy receptor organizes in dynamic protein complexes at the lysosomal membrane. *Mol. Cell. Biol.* **28**, 5747–5763 (2008).
62. Bandyopadhyay, U., Sridhar, S., Kaushik, S., Kiffin, R. & Cuervo, A. M. Identification of regulators of chaperone-mediated autophagy. *Mol. Cell* **39**, 535–547 (2010).
63. Dong, S. et al. Chaperone-mediated autophagy sustains haematopoietic stem-cell function. *Nature* **591**, 117–123 (2021).
64. Auzmendi-Iriarte, J. & Matheu, A. J. A. Intrinsic role of chaperone-mediated autophagy in cancer stem cell maintenance. *Autophagy* **18**, 3035–3036 (2022).
65. Eckerdt, F. et al. Combined PI3Kα-mTOR Targeting of Glioma Stem Cells. *Sci. Rep.* **10**, 21873 (2020).
66. Zhou, J. et al. Activation of the PTEN/mTOR/STAT3 pathway in breast cancer stem-like cells is required for viability and maintenance. *Proc. Natl. Acad. Sci. USA* **104**, 16158–16163 (2007).
67. Son, B., Lee, W., Kim, H., Shin, H. & Park, H. H. Targeted therapy of cancer stem cells: inhibition of mTOR in pre-clinical and clinical research. *Cell Death Dis.* **15**, 696 (2024).
68. Inoki, K., Li, Y., Zhu, T., Wu, J. & Guan, K.-L. TSC2 is phosphorylated and inhibited by Akt and suppresses mTOR signalling. *Nat. Cell Biol.* **4**, 648–657 (2002).
69. Li, G. et al. cGAS-STING pathway mediates activation of dendritic cell sensing of immunogenic tumors. *Cell. Mol. Life Sci.* **81**, 149 (2024).
70. Deng, L. et al. STING-Dependent Cytosolic DNA Sensing Promotes Radiation-Induced Type I Interferon-Dependent Antitumor Immunity in Immunogenic Tumors. *Immunity* **41**, 843–852 (2014).
71. Nakajima, S. et al. Radiation-Induced Remodeling of the Tumor Microenvironment Through Tumor Cell-Intrinsic Expression of cGAS-STING in Esophageal Squamous Cell Carcinoma. *Int. J. Radiat. Oncol., Biol., Phys.* **115**, 957–971 (2023).
72. Lv, J. et al. The tumor immune microenvironment of nasopharyngeal carcinoma after gemcitabine plus cisplatin treatment. *Nat. Med.* **29**, 1424–1436 (2023).
73. Ding, L. et al. PARP Inhibition Elicits STING-Dependent Antitumor Immunity in Brca1-Deficient Ovarian Cancer. *Cell Rep.* **25**, 2972–2980.e2975 (2018).
74. Wang, Q. et al. STING agonism reprograms tumor-associated macrophages and overcomes resistance to PARP inhibition in BRCA1-deficient models of breast cancer. *Nat. Commun.* **13**, 3022 (2022).
75. Dong, R. F. et al. Discovery of a potent inhibitor of chaperone-mediated autophagy that targets the HSC70-LAMP2A interaction in non-small cell lung cancer cells. *Br. J. Pharm.* **182**, 2287–2309 (2025).
76. Wang, Y. et al. Polyphyllin D punctures hypertrophic lysosomes to reverse drug resistance of hepatocellular carcinoma by targeting acid sphingomyelinase. *Mol. Ther.: J. Am. Soc. Gene Ther.* **31**, 2169–2187 (2023).
77. McCabe M. et al. Small molecule disruption of RARα/NCoR1 interaction inhibits chaperone-mediated autophagy in cancer. *EMBO molecular medicine*, (2025).
78. Qiu, H. et al. Efferocytosis: An accomplice of cancer immune escape. *Biomed. Pharmacother.* **167**, 115540 (2023).
79. Rochette, L. et al. Interplay between efferocytosis and atherosclerosis. *Arch. cardiovascular Dis.* **116**, 474–484 (2023).
80. Wang, E. J. et al. Targeting macrophage autophagy for inflammation resolution and tissue repair in inflammatory bowel disease. *Burns trauma* **11**, tkad004 (2023).
81. Werfel, T. A. & Cook, R. S. Efferocytosis in the tumor microenvironment. *Semin. Immunopathol.* **40**, 545–554 (2018).
82. Sanjuan, M. A. et al. Toll-like receptor signalling in macrophages links the autophagy pathway to phagocytosis. *Nature* **450**, 1253–1257 (2007).
83. Cunha, L. D. et al. LC3-Associated Phagocytosis in Myeloid Cells Promotes Tumor Immune Tolerance. *Cell* **175**, 429–441.e416 (2018).
84. Yang, S. et al. HIF1α/ATF3 partake in PGK1 K191/K192 succinylation by modulating P4HA1/succinate signaling in glioblastoma. *Neuro-Oncol.* **26**, 1405–1420 (2024).
85. Yi, K. et al. PTRF/cavin-1 remodels phospholipid metabolism to promote tumor proliferation and suppress immune responses in glioblastoma by stabilizing cPLA2. *Neuro-Oncol.* **23**, 387–399 (2021).
86. Tang, J. et al. TGF-β-activated lncRNA LINC00115 is a critical regulator of glioma stem-like cell tumorigenicity. *EMBO Rep.* **20**, e48170 (2019).
87. Huang, N. et al. An Upstream Open Reading Frame in Phosphatase and Tensin Homolog Encodes a Circuit Breaker of Lactate Metabolism. *Cell Metab.* **33**, 128–144.e129 (2021).
88. Chen, J. et al. Lnc-H19-derived protein shapes the immunosuppressive microenvironment of glioblastoma. *Cell Rep. Med.* **5**, 101806 (2024).
89. Subramanian, A. et al. Gene set enrichment analysis: a knowledge-based approach for interpreting genome-wide expression profiles. *Proc. Natl. Acad. Sci.* **102**, 15545–15550 (2005).
90. Ding, W., Feng, G., Hu, Y., Chen, G. & Shi, T. Co-occurrence and Mutual Exclusivity Analysis of DNA Methylation Reveals Distinct Subtypes in Multiple Cancers. *Front. Cell Dev. Biol.* **8**, 20 (2020).
91. Ding, W. et al. DNMIVD: DNA methylation interactive visualization database. *Nucleic acids Res.* **48**, D856–d862 (2020).
92. Ding, W., Chen, G. & Shi, T. Integrative analysis identifies potential DNA methylation biomarkers for pan-cancer diagnosis and prognosis. *Epigenetics* **14**, 67–80 (2019).
93. Goldman, M. J. et al. Visualizing and interpreting cancer genomics data via the Xena platform. *Nat. Biotechnol.* **38**, 675–678 (2020).
94. Zhao, Z. et al. Chinese Glioma Genome Atlas (CGGA): A Comprehensive Resource with Functional Genomic Data from Chinese Glioma Patients. *Genomics, Proteom. Bioinforma.* **19**, 1–12 (2021).
95. Gomez-Sintes, R. et al. Targeting retinoic acid receptor alpha-corepressor interaction activates chaperone-mediated autophagy

and protects against retinal degeneration. *Nat. Commun.* **13**, 4220 (2022).

96. Ohsumi, Y., Ishikawa, T. & Kato, K. A rapid and simplified method for the preparation of lysosomal membranes from rat liver. *J. Biochem.* **93**, 547–556 (1983).
97. Rodriguez-Navarro, J. A. et al. Inhibitory effect of dietary lipids on chaperone-mediated autophagy. *Proc. Natl. Acad. Sci. USA* **109**, E705–E714 (2012).
98. Juste, Y. R. & Cuervo, A. M. Analysis of Chaperone-Mediated Autophagy. *Methods Mol. Biol. (Clifton, NJ)* **1880**, 703–727 (2019).
99. Zhang, H. et al. Ammonia-induced lysosomal and mitochondrial damage causes cell death of effector CD8(+) T cells. *Nat. Cell Biol.* **26**, 1892–1902 (2024).
100. Cuervo, A. M., Dice, J. F. & Knecht, E. A population of rat liver lysosomes responsible for the selective uptake and degradation of cytosolic proteins. *J. Biol. Chem.* **272**, 5606–5615 (1997).
101. Wang, Z. et al. Fructose-1,6-bisphosphatase 1 functions as a protein phosphatase to dephosphorylate histone H3 and suppresses PPARα-regulated gene transcription and tumour growth. *Nat. Cell Biol.* **24**, 1655–1665 (2022).
102. Yang, W. et al. Nuclear PKM2 regulates β-catenin transactivation upon EGFR activation. *Nature* **480**, 118–122 (2011).

Acknowledgements

This work was supported by the National Natural Science Foundation of China (82273469; 32470752 to T.H.), Science, Technology and Innovation Commission of Shenzhen Municipality (JCYJ20220530143406014, JCYJ20250604122933044 to T.H.) and State Key Laboratory of Vaccines for Infectious Diseases, Xiang An Biomedicine Laboratory (2023XAKJ0101028 to T.H.). National Key R&D Program of China (2024YFA1107600 to J.L. and X.J.).

Author contributions

T.H. conceived the project, coordinated the study, and contributed to the design and interpretation of the experiments as well as to the writing of the manuscript. J.L. and X.J. played significant roles in developing this study. Y.L., M.S., W.L., and S.L. designed and conducted most of the experiments, analyzed and interpreted the data, and contributed to drafting the manuscript. B.W., B.L., M.L., X.Z., Q.X., S.H., and Z.Z. assisted with biological and biochemical experiments as well as data analysis. J.L., X.J., and S.-Y.C. provided essential reagents and valuable advice. All authors reviewed and edited the final draft of the manuscript.

Competing interests

The authors declare no competing interests.

Additional information

Supplementary information The online version contains supplementary material available at https://doi.org/10.1038/s41467-025-67119-3.

Correspondence and requests for materials should be addressed to Xiaobing Jiang, Junjun Li or Tianzhi Huang.

Peer review information *Nature Communications* thanks Hoang Van Phan and the other anonymous reviewer(s) for their contribution to the peer review of this work. A peer review file is available.